The Astrophysical Journal, 597:1211–1236, 2003 November 10
© 2003. The American Astronomical Society. All rights reserved. Printed in U.S.A.

RESONANT STRUCTURE IN THE KUIPER DISK: AN ASYMMETRIC PLUTINO DISK

Elizabeth K. Holmes
National Research Council Resident Research Associate, Jet Propulsion Laboratory, California Institute of Technology, MS 169-506, 4800 Oak Grove Drive, Pasadena, CA 91109;
elizabeth.holmes@jpl.nasa.gov

Stanley F. Dermott and Bo Å. S. Gustafson
Department of Astronomy, University of Florida, P.O. Box 112055, 211 Bryant Space Science Center, Gainesville, FL 32611;
dermott@astro.ufl.edu, gustaf@astro.ufl.edu

and

Keith Grogan
Jet Propulsion Laboratory, California Institute of Technology, MS 169-506, 4800 Oak Grove Drive, Pasadena, CA 91109;
keith.grogan@jpl.nasa.gov
Received 2002 August 29; accepted 2003 July 11

ABSTRACT

In order to develop a dynamical model of the Kuiper disk, we run numerical integrations of particles originating from source bodies trapped in the 3 : 2 external mean motion resonance with Neptune to determine what percentage of particles remain in the resonance for a variety of particle and source body sizes. The dynamical evolution of the particles is followed from source to sink with Poynting-Robertson light drag, solar wind drag, radiation pressure, the Lorentz force, neutral interstellar gas drag, and the effects of planetary gravitational perturbations included. We find that the number of particles in the 3 : 2 resonance increases with decreasing β (i.e., increasing particle size) for the cases in which the initial source bodies are small ($\leq$10 km in diameter) and that the percentage of particles in resonance is not significantly changed by either the addition of the Lorentz force, as long as the potential of the particles is small ($\approx$5 V), or the effect of neutral interstellar gas drag. The brightness of the entire Kuiper disk is calculated using a model composed of 500 μm diameter particles and fits well with upper limits to the Kuiper disk brightness and previous estimates. A disk with a size-frequency distribution weighted toward large particles, which are more likely to remain in resonance, may have a stronger, more easily identifiable resonant signature than a disk composed of small particles.

Subject headings: Kuiper Belt — solar system: general

On-line material: color figures

1. INTRODUCTION

In 1943 and 1951, respectively, Edgeworth and Kuiper independently speculated that planetary material may lie in our solar system beyond the orbit of Neptune (Jewitt 1999; Edgeworth 1943; Kuiper 1951). In 1992, Jewitt and Luu discovered 1992 QB1, the first object in what came to be known as the Kuiper Belt or the Edgeworth-Kuiper Belt (Jewitt & Luu 1993). As of 2003 March, more than 650 Kuiper Belt objects (KBOs) have been discovered (Trujillo & Brown 2002; Parker 2003[1]), which translates into an estimated 1×10^5 KBOs with diameters greater than 100 km (Jewitt 1999) orbiting with semimajor axes between 40 and 200 AU (Trujillo & Brown 2002). The Kuiper Belt was formed either because planet formation at those heliocentric distances did not occur as a result of the low density of planetesimals and the long encounter timescales between objects and/or because planetesimals were displaced into the region as a result of perturbing encounters with young Uranus and Neptune (Backman & Paresce 1993). In the asteroid belt, collisions between asteroids supply dust particles to the zodiacal cloud, the Sun's inner dust disk. By comparison, it has been postulated that collisions between KBOs could initiate a collisional cascade that would produce a Kuiper dust disk. In fact, the Kuiper Belt is the region of our solar system that is most analogous to the planetary debris disks we see around other stars such as Vega, β Pic, Fomalhaut, and ϵ Eri (Backman & Paresce 1993). In this paper we discuss some of the dynamical properties of the Kuiper Belt and the resonant structure of the Kuiper disk.

A Kuiper dust disk will have a resonant structure, with two concentrations in brightness along the ecliptic longitude (Dermott, Malhotra, & Murray 1988a; Liou & Zook 1999) arising because an estimated 6% of the Kuiper Belt objects are in the 3 : 2 mean motion resonance with Neptune (Trujillo & Brown 2002). Ultimately we want to develop a complete dynamical model of the Kuiper disk. The first step in this process is to run numerical integrations of particles originating from source bodies trapped in the 3 : 2 resonance and to determine what percentage of particles remain in the resonance for a variety of particle and source body sizes. Because the particle properties (shape, composition, etc.) are not well known, the variable we use to denote particle size is β, the magnitude of the ratio of the force of radiation pressure to the force of gravity. The dynamical evolution of the particles is followed from source to sink with Poynting-Robertson light drag (PR drag), solar wind drag, radiation pressure, the Lorentz force, neutral interstellar gas drag, and the effects of planetary gravitational perturbations included.

[1] The Distant EKOs Electronic Newsletter is available at http://www.boulder.swri.edu/ekonews.

Previous studies of particles in the Kuiper disk (Liou & Zook 1999; Moro-Martín & Malhotra 2002) are different from the study presented in this paper in three ways. Liou & Zook (1999) considered particles that originate outside of the 3 : 2 resonance and, by means of PR drag, can later become trapped in resonance. However, it may be more realistic to consider particles that originate from source bodies that are in the 3 : 2 resonance. This is especially important for large particles since they may suffer collisions that will quickly break them down into smaller particles before they can evolve into the 3 : 2 resonance. (Moro-Martín & Malhotra [2002] consider a range of initial semimajor axes: 35 AU $\leq a \leq$ 50 AU.) Secondly, Liou & Zook (1999) and Moro-Martín & Malhotra (2002) have not included the Lorentz force and neutral interstellar gas drag in their numerical integrations. Finally, we have included particles with $0 \leq \beta < 0.13$, while Liou & Zook (1999) considered particles with $0.05 \leq \beta \leq 0.4$ and Moro-Martín & Malhotra (2002) considered particles with $0.01 \leq \beta \leq 0.4$. Their particle distribution is weighted more toward smaller particles, yet they do not include the Lorentz force, which is more important for smaller particles.

We find that, for the cases in which the initial source bodies are small (i.e., $\leq$10 km in diameter), the number of particles in the 3 : 2 mean motion resonance increases with decreasing β (i.e., increasing particle size). Consequently, a size-frequency distribution for a Plutino disk must be weighted toward larger particles (i.e., those with smaller β-values). In addition, as long as the potential, U, of the particles is small ($U \approx 5$ V), the Lorentz force does not seem to prevent the particles from remaining in resonance. Similarly, the addition of the effect of neutral interstellar gas drag does not significantly change the percentage of particles remaining in resonance.

2. KUIPER BELT AND DISK

KBOs are divided into three dynamical classes: classical KBOs, scattered KBOs (SKBOs), and resonant KBOs. The orbits of the classical objects, which account for approximately two-thirds of the known KBOs, have semimajor axes 41 AU $\leq a \leq$ 47 AU and seem unassociated with resonances. They have moderate eccentricities ($e \approx 0.1$) and their inclinations lie in the range $0^\circ \leq I \leq 32^\circ$ (Jewitt 1999). Assuming that there are $\sim 10^5$ KBOs with diameters larger than 100 km, there are on the order of 50,000 classical KBOs in that size range (Jewitt 1999; Trujillo & Brown 2002).

Currently, approximately 10% of the observed KBOs are SKBOs (Trujillo & Brown 2002; Trujillo, Jewitt, & Luu 2000). The first member to be discovered, 1996 TL_{66}, has a semimajor axis of 85 AU, an eccentricity of 0.59, and an inclination of 24° (Luu et al. 1997). As a whole, the SKBOs are characterized by large eccentricities, large semimajor axes (>50 AU), and perihelia, q, near 35 AU because they were scattered by Neptune. The total number of SKBOs with diameters larger than 100 km is estimated to be on the order of 50,000 (Trujillo & Brown 2002). The SKBOs are thought to have been scattered by Neptune into a scattered disk (Trujillo et al. 2000). Finally, it should be noted that the observational techniques are biased toward lower inclinations, so the reported range of inclinations for these dynamical classes will be less than the actual range.

The resonant KBOs are primarily composed of the Plutinos, objects that reside in the 3 : 2 mean motion resonance with Neptune at a semimajor axis of 39.4 AU, and KBOs that reside in the 2 : 1 mean motion resonance with Neptune ($a \approx 47.7$ AU). The 4 : 3 and 5 : 3 resonances are also somewhat populated. We focus here on the 3 : 2 resonance. Pluto also resides in this resonance (Malhotra & Williams 1998) and, like the Plutinos, avoids close encounters with Neptune by being an aphelion librator. Approximately 15% of the observed KBOs are resonant KBOs. However, once the current observations are debiased, Plutinos (and KBOs in the other mean motion resonance with Neptune) probably compose 6% of the total KBO population (Trujillo & Brown 2002), or on the order of 6000 objects with diameters larger than 100 km. The eccentricities ($0.1 \leq e \leq 0.34$) and inclinations ($10^\circ \leq I \leq 20^\circ$) of the Plutinos bracket the values of Pluto ($e = 0.25$, $I = 17^\circ$).

As KBOs continue to be found, the existence of a Kuiper dust disk having an equilibrium grain population orbiting at approximately 30–50 AU has been postulated (Backman, Dasgupta, & Stencel 1995). As such a disk has not yet been directly observed, many theoretical questions remain about the size-frequency distribution of the particles in the disk, the evolution of the disk, and subsequent implications for the detectability of the Kuiper disk from existing or future observations. Such a disk could be generated in three ways: (1) by collisions between KBOs, (2) by impacts of interstellar dust grains onto KBOs, and (3) by mutual collisions between dust particles. Models of collisions between KBOs by Stern (1996) estimate a dust production rate in the Kuiper Belt of between 9.5×10^8 and 3.2×10^{11} g s^{-1}. These predictions are supported by observational evidence: the *Pioneer 10* and *Pioneer 11* spacecrafts have detected the signatures of Kuiper dust grains in the outer solar system (Landgraf et al. 2002). The dust detectors on board the *Pioneer* spacecraft registered detections due to particles in the size range of 10–6000 μm, too big to be interstellar grains. The *Pioneer 10* spacecraft detected a nearly constant flux of dust particles outside of Jupiter's orbit. Inside of Saturn's orbit, the dust particles are attributable to a combination of KBOs, short-period Oort cloud comets, and short-period Jupiter-family comets. However, to match the observations, Landgraf et al. (2002) conclude that the flux of dust particles outside of Saturn's orbit must be dominated by grains originating from the Kuiper disk. A Kuiper Belt dust production rate of approximately 5×10^7 g s^{-1} is needed to account for the amount of dust found by the *Pioneer* spacecrafts outside the orbit of Saturn. Yamamoto & Mukai (1998) estimate a total dust production rate of dust grains due to the impacts of interstellar grains with KBOs of 3.7×10^5 or 3.1×10^7 g s^{-1} depending on whether the surfaces of the KBOs are hard and icy or are covered by a layer of icy particles, respectively. Finally, Liou, Zook, & Dermott (1996) estimate that the average time for two 9 μm diameter Kuiper grains to have a mutual collision is 3.11×10^7 yr. In addition, for Kuiper grains starting out at 40 AU, Pepin, Palma, & Schlutter (2001) report a mean collisional survival time of between 2×10^6 and 10×10^6 yr for grains with diameters ranging from 10 to 10,000 μm. In fact, their 10 μm diameter grains succeed in penetrating to 1 AU. (In comparison, the PR drag lifetime for a 10 μm grain at 40 AU with density 2 g cm^{-2} is $\sim 4 \times 10^7$ yr for the geometrical optics case. The PR drag lifetime for a 10,000 μm grain is 4×10^{10} yr.) Since we only follow our numerical integrations for 2.5×10^5 yr, we neglect mutual collisions.

3. RESONANT STRUCTURE: MEAN MOTION RESONANCES

If a Kuiper disk exists, it would most likely have a resonant structure, with two concentrations in brightness along the ecliptic longitude (see Fig. 1). The structure arises from dust particles originating from the Plutinos, the KBOs trapped in the 3 : 2 mean motion resonance with Neptune, meaning that the particles orbit the Sun twice for every three times Neptune completes an orbit. We build a simple toy model of a Plutino disk, which is shown in Figure 1. The particles in the model are all one size: they are assumed to be large with $\beta = |\boldsymbol{F}_{\rm rad}|/|\boldsymbol{F}_{\rm grav}| \approx 0$. The particles' orbits are distributed through a three-dimensional array of cells, and a line-of-sight integrator allows the model to be viewed as it would appear in the 70 μm wave band in a coordinate frame that corotates with Neptune. Note the presence of the two lobes. A disk of particles trapped in a $p + 1 : p$ exterior mean motion resonance will have p lobes, which are located at the particles' pericenters. In the rotating frame, the lobes are caused by the fact that the angular velocity of the particles at pericenter becomes comparable to the angular velocity of Neptune (Murray & Dermott 1999). The position of Neptune would lie 90° from the two lobes, since the Plutinos are aphelion librators. Essentially, Figure 1 represents a snapshot of how the resonant cloud would appear, since the lobes corotate with Neptune; the positions of the lobes will change with time with respect to a non-Neptunian reference

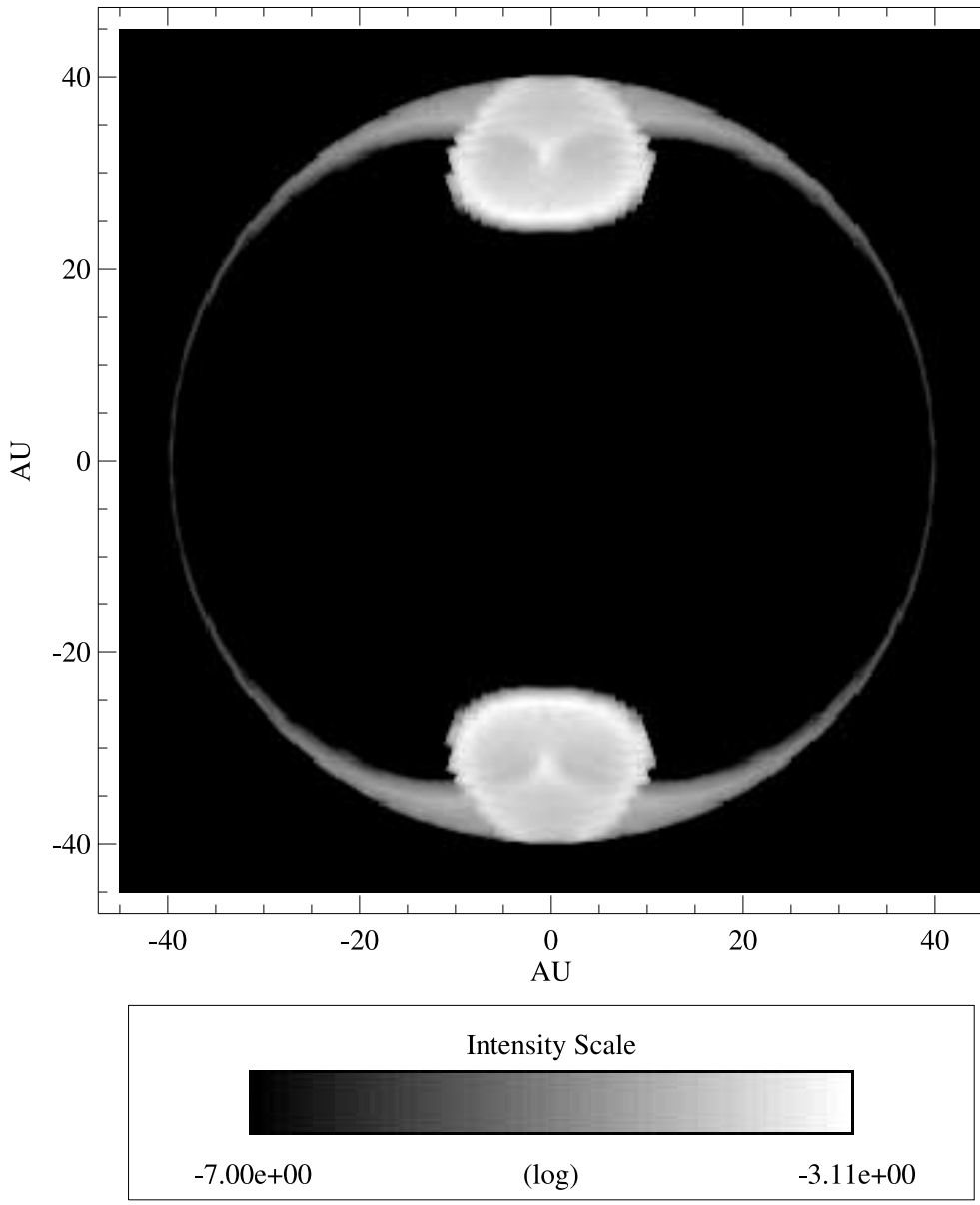

FIG. 1.—Toy model of a Plutino disk. The particles in the model are assumed to be large (≈300 μm in diameter) with $\beta \approx 0$. The particles' orbits are distributed through a three-dimensional array of cells, and a line-of-sight integrator allows the model to be viewed as it would appear in the 70 μm wave band in a coordinate frame that corotates with Neptune. Note the presence of the two lobes. A disk of particles trapped in a $p + 1 : p$ external mean motion resonance will have p lobes, which are located at the particle's pericenters. The position of Neptune would lie 90° from the two lobes, since the Plutinos are aphelion librators. The intensity is in arbitrary units of brightness, since the total brightness of the disk is not well determined. [*See the electronic edition of the Journal for a color version of this figure.*]

point. For example, in 2001 January Neptune's geocentric ecliptic longitude is ~126° (USNO and RGO 2001) and the geocentric ecliptic longitudes of the lobes would be 36° and 216°. In 2001 December Neptune's geocentric ecliptic longitude is ~128° and, correspondingly, the geocentric ecliptic longitudes of the lobes would be 38° and 218°, demonstrating that this signal is time varying. Since the Plutinos populate the densest and closest resonance to the inner edge of the Kuiper Belt, dust from these bodies would generate the brightest emission. This Plutino resonant ring is similar in nature to the resonant ring of dust particles corotating with the Earth (Jackson & Zook 1992; Dermott et al. 1994b; Jayaraman 1995), except that the lobes are symmetrical with respect to Neptune. There is no trailing cloud because the drag rate on the particles at ~40 AU is very small (Dermott et al. 1998). Shown in Figure 2 is a similar model to that shown in Figure 1 but with a nonzero libration width. The lobes are still visible but have a smoothed appearance.

Ultimately, the resonant structure in the Kuiper disk may be detectable using data from *COBE* or the *Space Infrared Telescope Facility* (*SIRTF*). The main impediment to detecting the Plutino ring is that, since it is located at approximately 39.4 AU, it will be very faint. Many brighter layers of emission will need to be subtracted from the data before the faint residuals can be studied for traces of the Plutino resonant structure. More promising may be the idea of detecting resonant structures in planetary debris disks. In Figure 3 we take the model shown in Figure 1 and show it as it would appear to *SIRTF* in the MIPS 70 μm wave band if the disk were located at 2 pc. Even with a pixel size of 1″, the lobes are still visible.

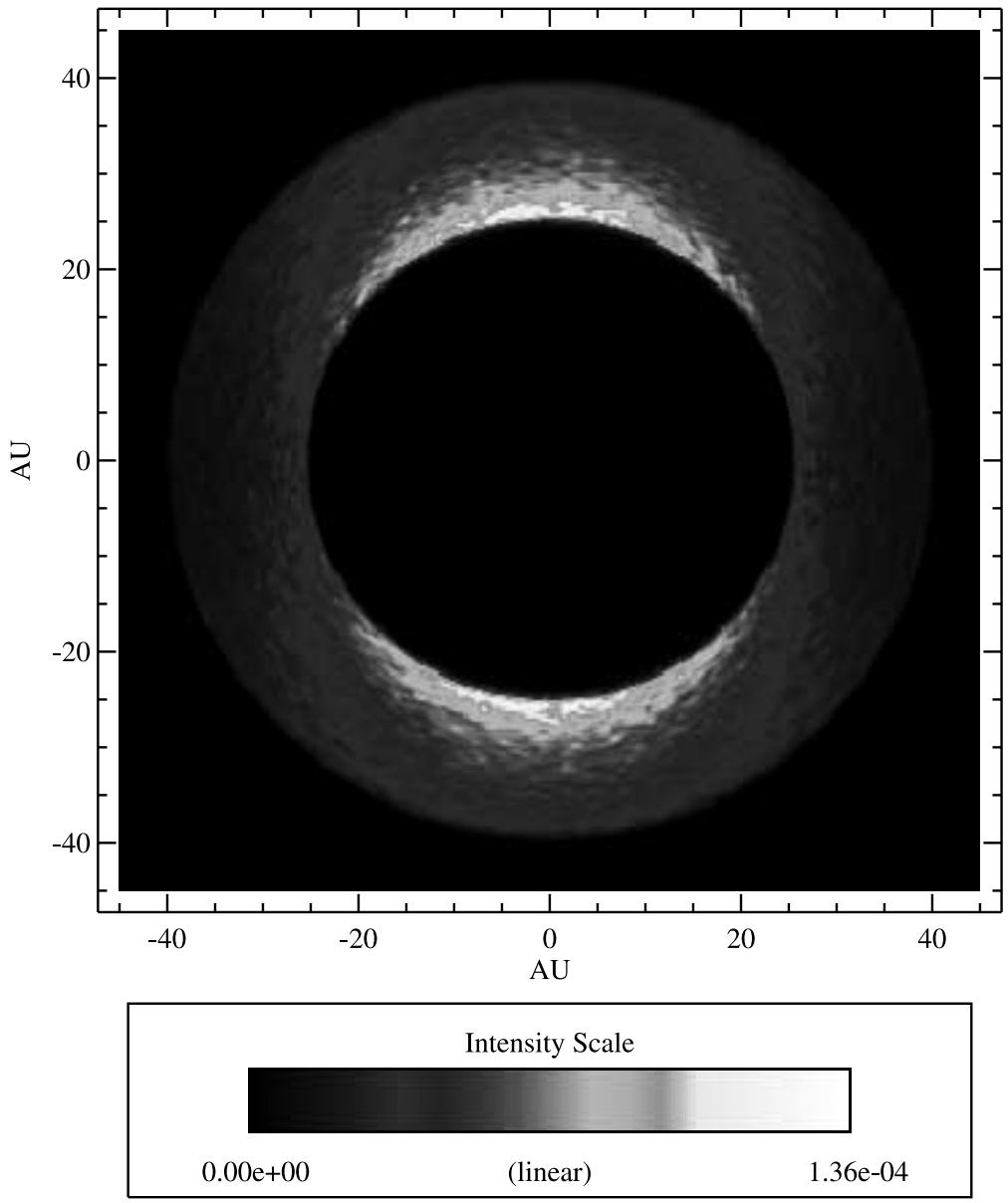

FIG. 2.—Toy model of a Kuiper disk from asteroidal particles (with a distribution of eccentricities and inclinations) in the 3 : 2 mean motion resonance with Neptune with a nonzero libration amplitude. This model is similar to that in Fig. 1 but with a nonzero libration width, which is represented by a Gaussian distribution of width ~30°. The two lobes are still visible but have a smoothed appearance. The intensity is in arbitrary units of brightness. [*See the electronic edition of the Journal for a color version of this figure.*]

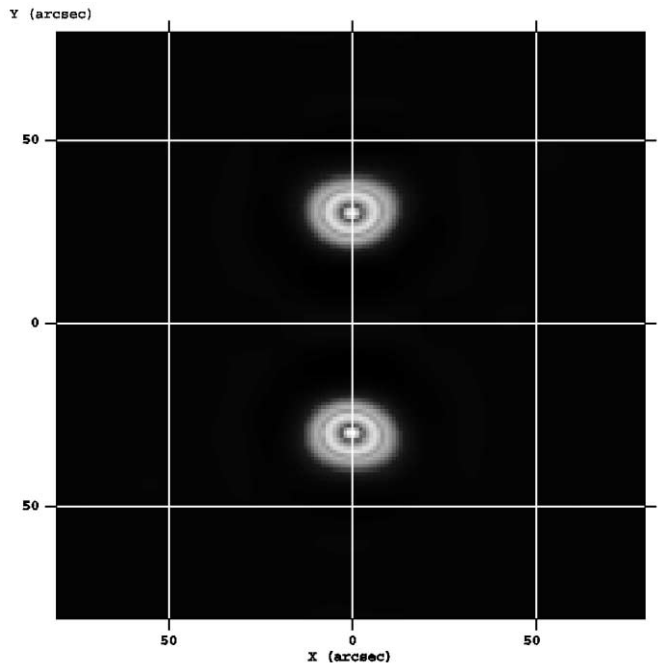

FIG. 3.—Toy model of the Plutino disk shown in Fig. 1 as it would appear to *SIRTF* in the MIPS 70 μm wave band if the disk were located at 2 pc. This image was constructed from 12 footprints. Each pixel is 1″ wide. The image, which has a linear scale and arbitrary intensity units, was produced using HiRes, a product of the Jet Propulsion Laboratory's Center for Long Wavelength Astrophysics. The two lobes are still visible. [*See the electronic edition of the Journal for a color version of this figure.*]

The models shown in Figures 1, 2, and 3 are very simplistic and are meant for illustrative purposes only. We have included a heuristic distribution of particle eccentricities and inclinations in the models and have not included any nongravitational forces, which need to be considered for particles less than $\sim$500 μm in diameter. The goal of the following sections is to calculate, first analytically and then numerically, the percentage of particles that stay in or become trapped in the 3 : 2 mean motion resonance for a given set of initial conditions to gain a more complete understanding of resonant structure in the Kuiper disk. We begin by discussing the forces that must be considered.

4. FORCES ON A DUST PARTICLE

A body, such as an asteroid or dust particle, orbiting a star possessing a planetary system is subject to three types of gravitational perturbations due to planets in the system: long-period or secular perturbations, resonant perturbations, and gravitational scattering by the planets. In addition, for dust particles $\leq$500–1000 μm in diameter, nongravitational forces must also be considered. In this section we give a brief overview of the nongravitational forces on a dust particle that are considered in our numerical simulations, namely, radiation pressure, PR drag, solar wind drag, the Lorentz force, and neutral interstellar gas drag. Different combinations of these forces are included in the dynamical models and numerical integrations in this paper. Another drag force, the Yarkovsky effect, typically only affects large bodies on the order of 1 m in diameter. Since our studies only encompass small micron-sized particles, we can omit the Yarkovsky effect from the following discussion. For a more complete discussion we refer the reader to Burns, Lamy, & Soter (1979) and Gustafson (1994).

The orbit of a particle or a planet can be described by a set of six osculating elements: the semimajor axis (a), eccentricity (e), inclination of the orbit to a reference plane (I), longitude of ascending node (Ω), longitude of pericenter ($\tilde{\omega}$), and the mean longitude (λ). The forces below are calculated for the case of the solar system, but it is trivial to derive expressions for an exosolar system case. In general, forces on a dust particle can be separated into two categories: gravitational and nongravitational forces. The gravitational forces will be discussed in more detail in a subsequent section on mean motion resonances.

4.1. *Radiation Pressure*

Particles are affected by photons streaming out from the Sun. These photons act on the particles, producing a repulsive force known as the radiation pressure force, $\boldsymbol{F}_{\rm rad}$. A dimensionless quantity, β, is used to describe radiation pressure. It is defined as the ratio of the radiation pressure force to the force of gravity: $\beta = |\boldsymbol{F}_{\rm rad}|/|\boldsymbol{F}_{\rm grav}|$. The force of gravity can be written as $\boldsymbol{F}_{\rm grav} = -(GMm/r^2)\hat{\boldsymbol{r}}$, where $G = 6.67 \times 10^{-11}$ N m^2 kg^{-2} is the gravitational constant, M is the mass of the Sun ($M_\odot = 1.99 \times 10^{30}$ kg) or, in general, the central star, r is the heliocentric distance, and m is the mass of an individual dust particle. If we combine the forces of gravity and radiation pressure, the resulting total force on the particle is

$$\boldsymbol{F} = -\frac{G(1-\beta)Mm}{r^2}\hat{\boldsymbol{r}}\,, \tag{1}$$

which means that when a particle is acted upon by radiation pressure, the gravitational pull on the particle is equivalent to that of the Sun if its mass were reduced by a factor of $(1-\beta)$ (Burns et al. 1979; Gustafson 1994).

4.2. *Poynting-Robertson Light Drag*

When a particle absorbs incident radiation from the Sun, it reradiates (or scatters) it isotropically in the particle's rest frame. However, since the particle is moving with respect to the Sun, according to special relativity the particle does not reradiate (or scatter) the energy flux isotropically in the rest frame of the Sun. The particle reradiates (or scatters) more energy in the direction of its velocity than in the opposite direction, causing a loss of momentum. Since the mass of the particle is constant, this loss of momentum translates into a deceleration of the particle, resulting in a net drag on the particle. The drag effect is referred to as PR drag (Poynting 1903; Robertson 1937; Burns et al. 1979). The loss of momentum causes the particle to move to a lower orbit, resulting in the particle slowly spiraling into the Sun over a period of time called the PR drag lifetime (Burns et al. 1979). To the first order in v/c, the total radiation force (radiation pressure force combined with PR drag) acting on a spherical particle is

$$|\boldsymbol{F}_{\rm grav}|\beta\left[1\hat{\boldsymbol{r}} - \left(\frac{2\dot{r}}{c}\right)\hat{\boldsymbol{r}} - \left(\frac{r\dot{\theta}}{c}\right)\hat{\boldsymbol{\theta}}\right]\,, \tag{2}$$

where the unit vector $\hat{\boldsymbol{\theta}}$ is normal to $\hat{\boldsymbol{r}}$ in the orbital plane (Burns et al. 1979; Klacka 1992; Gustafson 1994). The first term is the radiation pressure force already discussed above, and both the second and third terms are PR drag. Since PR

drag is a radial force, the inclination and the ascending node are not affected and the change in longitude of perihelion is negligible for small eccentricities. Given below are the changes in semimajor axis and eccentricity with respect to time where $\alpha_{\rm PR} = GM_{\odot}/c$ (Wyatt & Whipple 1950):

$$\frac{da}{dt} = -\frac{\alpha_{\rm PR}\beta}{a}\frac{(2+3e^2)}{(1-e^2)^{3/2}} , \tag{3}$$

$$\frac{de}{dt} = -\frac{5\alpha_{\rm PR}\beta}{2a^2}\frac{e}{(1-e^2)^{1/2}} . \tag{4}$$

4.3. *Solar Wind Corpuscular Drag*

Another nongravitational force acting on dust particles is the force due to solar wind corpuscular drag, $\boldsymbol{F}_{\rm sw}$, which is caused by solar wind protons streaming out from the Sun and impacting the particles in their paths. $\boldsymbol{F}_{\rm sw}$ is analogous to the total radiation force given in equation (2). We can define $\beta_{\rm sw}$ to be equal to $\beta_{\rm sw} = |\boldsymbol{F}_{\rm sw}|/|\boldsymbol{F}_{\rm grav}|$. Taking $v_{\rm sw}$ to be the solar wind speed, we can write the solar wind force as

$$\boldsymbol{F}_{\rm sw} = \left|\boldsymbol{F}_{\rm grav}\right|\beta_{\rm sw}\left[1\hat{\boldsymbol{r}} - \left(\frac{2\dot{r}}{v_{\rm sw}}\right)\hat{\boldsymbol{r}} - \left(\frac{r\dot{\theta}}{v_{\rm sw}}\right)\hat{\boldsymbol{\theta}}\right] , \tag{5}$$

which has the same form as equation (2) (Gustafson 1994). We can approximate the solar wind drag force as being roughly $\frac{1}{3}$ the value of the total radiation force given in equation (2).

4.4. *Solar Wind Lorentz Force*

Interplanetary dust particles are charged and as a result are coupled to the solar wind–driven interplanetary magnetic field. The particles acquire a charge by a variety of methods: the photoemission of electrons from the absorption of ultraviolet (UV) solar radiation and the accretion of solar wind protons tends to positively charge the particles, while the accretion of solar wind electrons imparts a negative charge to the dust grains. The equation for the equilibrium charge state can be written as

$$\sigma_e(U) f_e = \sigma_p(U) f_p + y\sigma_{\rm ph} f_{\rm ph} , \tag{6}$$

where σ_e, σ_p, and $\sigma_{\rm ph}$ are the cross sections of the grains for electrons, protons, and UV photons, respectively, the f-values are the corresponding fluxes, and y is the photoelectron yield (Gustafson & Misconi 1979). It is predicted that under normal conditions, photoemission dominates over the accretion of solar wind particles, giving the dust particles a net positive potential, U, of $\approx$5 V (Goertz 1989; Gustafson 1994). This potential is independent of distance since solar wind density follows an approximate $1/r^2$ decrease in density (Leinert & Grün 1990), and it corresponds to a charge $q = 4\pi\epsilon_0 Us$ on a spherical particle where $\epsilon_0 = 8.859 \times 10^{-12}$ C V^{-1} m^{-1}. The force exerted on the particle by the interplanetary magnetic field, $\boldsymbol{B}$, can be written as

$$\boldsymbol{F}_{\rm L} = q\boldsymbol{v} \times \boldsymbol{B} , \tag{7}$$

where $\boldsymbol{v}$, the velocity with respect to this field, can be broken down into components $\boldsymbol{v}_g$, the heliocentric velocity of the particle, and $\boldsymbol{v}_{\rm sw}$, the solar wind velocity:

$$\boldsymbol{F}_{\rm L} = q(\boldsymbol{v}_g \times \boldsymbol{B} - \boldsymbol{v}_{\rm sw} \times \boldsymbol{B}) . \tag{8}$$

This is the classical representation of the Lorentz force. The second term in the above equation is independent of the particle's motion and can be viewed as resulting from an induced electric field. Gustafson & Misconi (1979) found that although solar wind parameters are variable and uncertain over long timescales, this second term is stable in magnitude and direction. Gustafson & Misconi (1979) and more recently Grogan, Dermott, & Gustafson (1996) modeled the magnetic field, utilizing the expanding solar corona model of the solar magnetic field (Parker 1958). In Parker's model, the gas flowing outward from the solar corona draws out the solar magnetic field lines as the Sun rotates, so that close to the Sun the field is approximately radial, but farther from the Sun the field lines form an Archimedean spiral (Grogan et al. 1996; Gustafson 1994). In the following equations, B_0 is the magnetic field strength at some reference distance, b ($B_0 \sim 3$ nT), ω is the angular velocity of the Sun ($\omega \approx 2.7 \times 10^{-6}$), r is the radial distance from the Sun, ϕ is the azimuth angle, and θ is the heliocentric colatitude angle; the solar wind velocity, $v_{\rm sw}$, is taken to be 400 km s^{-1}:

$$B_r = \frac{B_0}{r^2} , \tag{9}$$

$$B_\phi = \frac{-B_0\omega b^2(r-b)\sin\theta}{v_{\rm sw}r^2} , \tag{10}$$

$$B_\theta = 0 . \tag{11}$$

The above equations are derived using the velocity of the gas flowing out from the Sun, v, where $v_r = v_{\rm sw}$, $v_\phi = \omega(r-b)\sin\theta$, and $v_\theta = 0$ (Parker 1958).

4.5. *Neutral Interstellar Gas Drag*

This last force, while small in magnitude, acts from a specific direction and could potentially cause noticeable effects on the orbits of dust particles over a large period of time. The solar system inhabits a "Local Bubble" in the local interstellar medium (LISM) consisting of hot plasma (10^6 K) of very low density (5×10^{-3} cm^{-3}) that spans roughly 100 pc. It is thought that this void was created by a supernova explosion (Gehrels & Chen 1993; Grün et al. 1994). Within the Local Bubble lies the "Local Fluff," consisting of several clouds a few parsecs wide having higher densities and cooler temperatures than those of the Local Bubble, and within the Local Fluff lies our solar system. The cloud in which the Sun resides has a temperature of 10^4 K and a density of 0.1 H atoms cm^{-3} (Bertin et al. 1993; Grün et al. 1994). The interaction of the solar wind with the LISM causes a cavity to form, which extends out to approximately 100 AU and is termed the heliosphere. Inside the heliosphere only neutral gas atoms, primarily hydrogen, reach the planetary system since interstellar ions are removed from the solar system by the solar wind (Geiss, Gloeckler, & Mall 1994; Gloeckler et al. 1993; Grün et al. 1994).

The *Ulysses* spacecraft has detected a stream of interstellar helium (Witte et al. 1993; Grün et al. 1994), a tracer of hydrogen, originating from an ecliptic longitude of 252° and an ecliptic latitude of +2°.5 moving with a speed of 26 km s^{-1} (Witte et al. 1993; Grün et al. 1994), which is in good agreement with the direction of motion of the local cloud in which the Sun is embedded with respect to the solar system (Bertin et al. 1993). These neutral gas atoms can collide with dust grains in the solar

system, causing a change in the momentum of the dust particles. While the effects of one collision are negligible, over a period of time repeated collisions have the potential to alter the orbital elements of the dust particle significantly (Scherer 2000).

For a spherical dust grain with radius s, mass m, and velocity $\boldsymbol{v}$, the drag force, $\boldsymbol{F}_{\rm H}$, on the dust particle due to collisions with neutral interstellar hydrogen particles of mass $m_{\rm H}$ moving with a velocity $\boldsymbol{v}_{\rm H}$ can be written as

$$\boldsymbol{F}_{\rm H} = -Nm_{\rm H}u\hat{\boldsymbol{u}} \, , \tag{12}$$

where $\boldsymbol{u} = \boldsymbol{v} - \boldsymbol{v}_{\rm H}$, $u = |\boldsymbol{v} - \boldsymbol{v}_{\rm H}|$, $\hat{\boldsymbol{u}}$ is the unit vector in the u-direction, and N, the average number of collisions of hydrogen atoms on a dust particle of collisional cross-sectional area, σ, per unit time, is defined as

$$N = n_{\rm H}\sigma u C_D \, , \tag{13}$$

where $n_{\rm H}$ is the number density of hydrogen atoms, $\sigma = \pi s^2$, where s is the radius of the dust particle, and C_D is the free molecular drag coefficient due to hydrogen atoms in a Maxwellian velocity distribution of temperature $T_{\rm H}$ impacting a spherical dust particle (Gustafson 1994; Scherer 2000), where $T_{\rm H} \sim 8000$ K. Substituting equation (13) into equation (12) gives

$$\boldsymbol{F}_{\rm H} = -n_{\rm H}\pi s^2 m_{\rm H}|\boldsymbol{v} - \boldsymbol{v}_{\rm H}|^2 C_D\hat{\boldsymbol{u}} \, , \tag{14}$$

where the numerical values of the constants are as follows: $n_{\rm H} = 0.1$ H atoms cm^{-3}, s is a range of sizes, $m_{\rm H} = 1.675 \times 10^{-24}$ g, the particle velocity, $\boldsymbol{v}$, is calculated at each time step in numerical integrations, $\boldsymbol{v}_{\rm H}$ is 26 km s^{-1}, and C_D, the free molecular drag coefficient, is roughly 1–2 (Gustafson 1994). The value of C_D varies with the type of collision that is assumed to occur and also with the particle shape and orientation. For instance, a C_D of 2 corresponds to the case in which the total momentum of a proton that hits the dust particle is transferred to the particle (Gustafson 1994). We do not want to limit our calculations by making too many assumptions and have elected to run simulations with $C_D = 1$ and 2.

4.6. *Collisions*

Collisions between dust particles will also affect some dust particles. For small particles ($\lesssim 100$ μm) in the asteroid belt, collisions are not important since their collisional lifetimes are much longer than their PR drag lifetimes. Leinert & Grün (1990) estimate the average impact speed between two dust particles as

$$\langle v(r)\rangle = v_0\left(\frac{r}{r_0}\right)^{-0.5} \, , \tag{15}$$

where $v_0 = 20$ km s^{-1} at $r_0 = 1$ AU. The rate $C(m, r)$ of catastrophic collisions, collisions that result in the fragmentation of both particles, is given by

$$C(m, r) = \int_{m/\gamma(v(r))}^{\infty} \sigma n(m_p, r)\langle v(r)\rangle dm_p \, , \tag{16}$$

where σ is the cross-sectional area inside the circle where the two particles touch, m_p is the mass of the projectile, $n(m_p, r)$ is the number density of particles of mass m at heliocentric distance r, and $\gamma(v(r))$ is defined by

$$m_p \geq \frac{1}{\gamma(v(r))} M_t \, , \tag{17}$$

where M_t is the mass of the target particle (Leinert & Grün 1990). The collisional lifetime of a particle is defined as

$$\tau_c = \frac{1}{C(m, r)} \, , \tag{18}$$

the reciprocal of the rate of catastrophic collisions (Leinert & Grün 1990). Hence, roughly speaking, $n(m_p, r) \sim r^{-3}$, $\langle v(r)\rangle \sim r^{-0.5}$, so $C(m, r) \sim r^{-3.5}$ making $\tau_c \sim r^{3.5}$. The PR drag lifetime only goes as $\tau_{\rm PR} \sim a^2 \sim r^2$. Since the collisional lifetime at heliocentric distance r is a steeper function of r than the PR drag lifetime, we can make the assumption that the collisional lifetime of particles at r is longer than their PR drag lifetime. We can assume that collisions can be neglected for small particles at a distance r from the Sun. However, we know that collisions do become important for particles larger than ~ 100 μm in diameter (Gustafson et al. 1992) and will need to be considered in future work.

4.7. *Comparisons of Forces*

We calculate the magnitude of various forces (in newtons) on dust particles of different β-values (assuming that the particles are spheres with diameter d) and present them in Table 1, assuming that a given particle has a density of $\rho = 2.5$ g cm^{-3}, a mass of $m_{\rm dust}$, a semimajor axis a where $a = r = 39.4$ AU, and an eccentricity $e = 0$. In this case, the heliocentric velocity of the particle is given by $v = [GM_\odot(1 - \beta)/a]^{1/2}$ in km s^{-1}. The mass of the Sun, $M_\odot$, is taken to be 1.99×10^{30} kg. The solar wind velocity is taken to be 400 km s^{-1}, and B_0 is ~ 3 nT $= 3 \times 10^{-9}$ N s m^{-1} C^{-1}. The charge, q, on the dust particle is $q = 4\pi\epsilon_0 Ud/2$, where $\epsilon_0 = 8.86 \times 10^{-12}$ C V^{-1} m^{-1} is the permeability of a vacuum. $\boldsymbol{F}_{\rm grav}$ is the force of gravity. The magnitude of the force due to radiation pressure, $|\boldsymbol{F}_{\rm rad}|$, is simply $\beta|\boldsymbol{F}_{\rm grav}|$. The force due to PR drag, $\boldsymbol{F}_{\rm PR}$, is represented by the second and third terms in equation (2). The Lorentz force, $\boldsymbol{F}_{\rm L}$, is defined in equation (8), and for the above calculations, we chose the azimuth angle, ϕ, to be 0° and the heliocentric colatitude angle, θ, to be 20°. Finally, $\boldsymbol{F}_{\rm H}$, the force due to neutral interstellar gas particles impacting the dust grains, is given by equation (14). Additional constants and assumptions are given in Holmes (2002).

TABLE 1

MAGNITUDE OF VARIOUS FORCES ON 10 AND 100 μm DIAMETER SPHEROIDAL DUST PARTICLES

PARAMETER	SPHERE DIAMETER	
	10 μm	100 μm
$\beta = \lvert\boldsymbol{F}_{\rm rad}\rvert/\lvert\boldsymbol{F}_{\rm grav}\rvert$	0.04868	0.00446
$a = r$ (AU)	39.4	39.4
$m_{\rm dust}$ (kg)	1.3×10^{-12}	1.3×10^{-9}
$\lvert\boldsymbol{F}_{\rm grav}\rvert$ (N)	5.0×10^{-18}	5.0×10^{-15}
$\lvert\boldsymbol{F}_{\rm rad}\rvert$ (N)	2.4×10^{-19}	2.2×10^{-17}
$\lvert\boldsymbol{F}_{\rm PR}\rvert$ (N)	9.3×10^{-24}	8.7×10^{-22}
$\lvert\boldsymbol{F}_{\rm L}\rvert$ ($U = 5$ V) (N)	2.9×10^{-20}	2.9×10^{-19}
$\lvert\boldsymbol{F}_{\rm L}\rvert$ ($U = 20$ V) (N)	1.2×10^{-19}	1.2×10^{-18}
$\lvert\boldsymbol{F}_{\rm H}\rvert$ ($C_D = 1$) (N)	1.2×10^{-23}	1.2×10^{-21}

TABLE 2
RATIOS OF THE MAGNITUDE OF THE FORCES ON A 10 ($\beta = 0.04868$) AND 100 μm ($\beta = 0.00446$) DUST PARTICLE

PARAMETER	SPHERE DIAMETER	
	10 μm	100 μm
$\lvert F_{rad}/F_{grav}\rvert = \beta$	4.9×10^{-2}	4.5×10^{-3}
$\lvert F_{PR}/F_{grav}\rvert$	1.9×10^{-6}	1.7×10^{-7}
$\lvert F_{L}/F_{grav}\rvert$ ($U = 5$ V)	5.9×10^{-3}	5.9×10^{-5}
$\lvert F_{L}/F_{grav}\rvert$ ($U = 20$ V)	2.3×10^{-2}	2.3×10^{-4}
$\lvert F_{H}/F_{grav}\rvert$ ($C_D = 1$)	2.5×10^{-6}	2.5×10^{-7}

The ratios of the forces in Table 1 are shown in Table 2. In the case of the 10 μm diameter Kuiper disk particle, we see that $\lvert F_{rad}/F_{grav}\rvert$ is the same order of magnitude as $\lvert F_{L}/F_{grav}\rvert$ for $U = 20$ V and almost the same order of magnitude for $U = 5$ V. However, for the 100 μm particle, $\lvert F_{rad}/F_{grav}\rvert$ is at least an order of magnitude greater than $\lvert F_{L}/F_{grav}\rvert$ for both potentials, making the Lorentz force less important for larger particles. For both the 10 and 100 μm size particles, $\lvert F_{PR}/F_{grav}\rvert$ is the same order of magnitude as $\lvert F_{H}/F_{grav}\rvert$ and in both cases the ratio is 4 orders of magnitude less than $\lvert F_{rad}/F_{grav}\rvert$.

5. THE DYNAMICS OF MEAN MOTION RESONANCES

Consider two large objects moving around a large, central mass in circular, coplanar orbits. For now, we assume that $\beta = 0$. The outer object (primed) is said to move in resonance with the inner object, if their mean motions, n' and n, respectively, can be related as

$$\frac{n}{n'} = \frac{p+q}{p} , \tag{19}$$

where p and q are integers, q denoting the order of the resonance. Since the mean motion can be related to the semimajor axis by $\mu_\odot = GM_\odot = n^2a^3$, the following relation can be written:

$$a' = a\left(\frac{p+q}{p}\right)^{2/3} . \tag{20}$$

Following the derivations given in Dermott et al. (1988a), Weidenshilling & Jackson (1993), Jayaraman (1995), and Murray & Dermott (1999), if we consider only the resonant terms, the perturbing force on a particle due to a planet can be written as a series expansion in the orbital elements of the planet $(a, e, I, \Omega, \tilde{\omega}, \lambda)$ and the particle $(a', e', I', \Omega', \tilde{\omega}', \lambda')$:

$$R'_{res} = \mu \sum S'(a, e, I, a', e', I') \cos\varphi , \tag{21}$$

where $\mu = GM$, G is the gravitational constant, and M is the mass of the planet. The strength of the resonance, S', the strength of an individual term in the series, can be written as $S' = S'(\alpha, \sin I, \sin I', e, e')$, where $\alpha = (a/a')$. The general form of the resonant argument, φ, can be written as

$$\varphi = j_1\lambda' + j_2\lambda + j_3\tilde{\omega}' + j_4\tilde{\omega} + j_5\Omega' + j_6\Omega , \tag{22}$$

where $j_1 = (p+q)$, $j_2 = -q$, and the primed quantities denote those orbital elements of the external orbiting body and the unprimed quantities denote those of the interior body. Physically, the resonant argument can be thought of as the angular distance between the particle's perihelion and the longitude of conjunction of the particle with the planet. We will retain the primes in the subsequent discussion so that the orbital elements of the planet, in this case Neptune, will be denoted as $(a_N, e_N, I_N, \Omega_N, \tilde{\omega}_N, \lambda_N)$ and those of the Plutinos and dust particles associated with the Plutinos as $(a', e', I', \Omega', \tilde{\omega}', \lambda')$. This distinction is important to make since the disturbing functions are different for interior and external resonances, and so the derivation of libration width depends on whether the resonance is interior or exterior. Also note that if $p = 1$, an extra term must be included in the disturbing function. However, since we are dealing with the 3 : 2 resonance, a $p = 2$ resonance, we need not include that term in our derivation.

5.1. *First-Order External Resonances in the Circular Restricted Three-Body Problem*

For exact first-order external resonances $|j_3| = 1 = q$, and j_4, j_5, and j_6 are zero, giving

$$\varphi = (p+1)\lambda' - p\lambda_N - \tilde{\omega}' , \tag{23}$$

if we take j_3 to be -1. Now we write the general term in the averaged expansion of the disturbing function, with both secular and resonant terms included. Equation (21) becomes

$$\langle R'_{res}\rangle = \frac{GM_N}{a_N}\alpha\left[f_{s,1}(\alpha)e'^2 + f_d(\alpha)e'^{|j_3|}\cos\varphi\right] . \tag{24}$$

The first term on the right-hand side is the secular term, which depends on $f_{s,1}(\alpha)$. The second term is the resonant term, and it is a function of $f_d(\alpha)$. Both $f_{s,1}(\alpha)$ and $f_d(\alpha)$ are functions of Laplace coefficients and are defined in Murray & Dermott (1999). The term containing $f_{s,1}(\alpha)$ will be eventually neglected. For the 3 : 2 external mean motion with Neptune, the resonant argument is

$$\varphi = 3\lambda' - 2\lambda_N - \tilde{\omega}' . \tag{25}$$

For first-order external resonances, $j_3 = -1$ and the relationship for the libration width is

$$\delta a'_{max} = \pm\left[\sqrt{\left(\frac{16|C'_r|\alpha}{3n'}e'\right)\left(1 + \frac{1}{27j_1^2e'^3}\frac{|C'_r|\alpha}{n'}\right)} - \frac{2}{9j_1e'}\frac{|C'_r|\alpha}{n'}\right]a' , \tag{26}$$

where

$$C'_r = \left(\frac{GM_N}{a'^2a_Nn'}\right)f_d(\alpha) , \tag{27}$$

where M_N is the mass of Neptune and G is the solar gravitational constant. The full derivation of the libration width using the pendulum model is given in Murray & Dermott (1999). Figure 4 shows the maximum libration widths, calculated using equation (26), in a-e space for the 3 : 2 external mean motion resonance with Neptune.

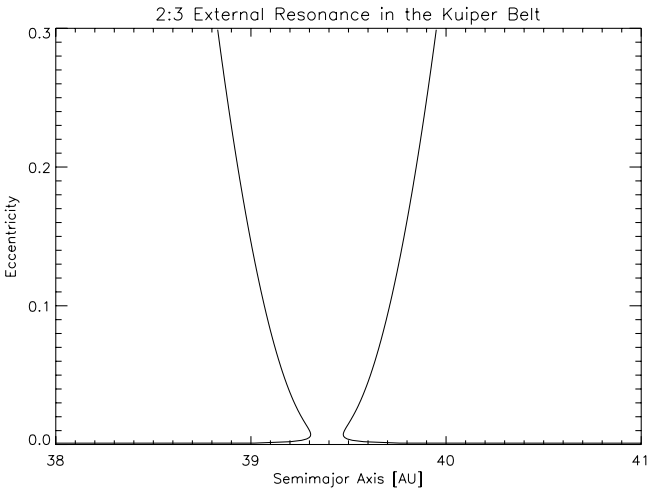

FIG. 4.—Maximum libration widths in *a*-*e* space for the 3:2 external mean motion resonance with Neptune.

6. SOURCE BODIES

Particles are generated in the Kuiper Belt by the breakup of KBOs. If a parent body has orbital elements (a_s, e_s, I_s, Ω_s, $\tilde{\omega}_s$), then immediately after breakup the collisional byproducts of that parent body have a range of orbital elements (Δa, Δe, ΔI, $\Delta\Omega$, $\Delta\tilde{\omega}$). We can determine if particles will stay in a given resonance by comparing Δa with the libration width, $\delta a'_{\max}$, for that particular resonance. If

$$\Delta a < \delta a'_{\max} , \tag{28}$$

then particles will stay in the resonance, at least initially. We can calculate Δa by making the following simple assumptions. Ejection velocities immediately after impact, $V_{\rm ej}$, for fragments of asteroid collisions are given by the relation

$$V_{\rm ej} = \sqrt{V_\infty^2 + V_{\rm esc}^2} , \tag{29}$$

where V_∞ is the velocity of the fragments at infinity and $V_{\rm esc}$ is the escape velocity from the parent body (Zappala et al. 1984; Cellino et al. 1999). To escape the parent body, a fragment must have an ejection velocity that is at least equal to the escape velocity. Otherwise, the fragment will reimpact the parent body, forming a regolith in the case of small particles. The escape velocity is not the same for all of the fragments; it depends on the size of the fragment, the initial radial location of each fragment with respect to the center of the parent body, and the ejection process. For example, the largest remaining fragment may have an escape velocity close to zero (Cellino et al. 1999). Various authors calculate a guaranteed escape speed, the speed at which a fragment launched normal to the surface of its parent body will have enough energy to escape the parent body, taking into account that each parent body will have a unique shape and rotation rate and therefore a unique gravitational field (Scheeres, Durda, & Geissler 2003). For example, asteroid 433 Eros has approximate dimensions of $34 \times 13 \times 13$ km (Veverka et al. 2001) and has a range of guaranteed escape speeds from 3.3 to 17.3 m s^{-1} (Scheeres et al. 2003; Yeomans et al. 2000; Miller et al. 2002). However, this detailed analysis is beyond the scope of this paper and we follow Cellino et al. (1999), who parameterized the escape velocity in the following simplified way:

$$V_{\rm esc} = v_{\rm esc}\left(1 - \frac{d}{R_s}\right) , \tag{30}$$

where d is the diameter of the fragment, R_s is the radius of the parent body, and $v_{\rm esc}$ is the full escape velocity from the parent body given by

$$v_{\rm esc} = \sqrt{\frac{2GM_s}{R_s}} , \tag{31}$$

where M_s is the mass of the parent body. If we assume that the parent body is spherical and take ρ_s to be its density, we can rewrite equation (31) as $v_{\rm esc} = R_s[(8\pi G\rho_s)/3]^{1/2}$. In the case we are considering, that of micron-sized dust particles, $d \ll R_s$ in equation (30) and therefore $V_{\rm esc} \approx v_{\rm esc}$. Deriving an effective diameter for Eros of 17.9 km and assuming $\rho = 2.5$ g cm^{-3}, we calculate $V_{\rm esc} = 10.6$ m s^{-1} for Eros, which is very close to the average guaranteed escape speed of 10.3 m s^{-1} derived by Scheeres et al. (2003), Yeomans et al. (2000), and Miller et al. (2002).

We take Δv_t, Δv_r, and $\Delta v_\perp$ to be the dispersions in the tangential, radial, and perpendicular components of the particles' velocities upon ejection. If we assume that the collisions disperse particles isotropically, the average components of the velocity dispersion are equal to each other (Zappala et al. 1984; Cellino et al. 1999):

$$\Delta v_t \cong \Delta v_r \cong \Delta v_\perp \cong \frac{V_\infty}{\sqrt{3}} . \tag{32}$$

This assumption may seem too simplistic since fragments ejected with a small Δv_t will have their ejection velocities underestimated. However, fragments with small Δv_r and $\Delta v_\perp$ components will have their ejection velocities slightly overestimated. From a statistical point of view these over- and underestimates should average out (Cellino et al. 1999). Since it is difficult to estimate $V_{\rm ej}$, we make the simplifying assumption, following Zappala et al. (1984), that $V_{\rm ej} = \sqrt{2}V_{\rm esc}$. We can now write

$$\Delta v_t \cong \Delta v_r \cong \Delta v_\perp \cong \frac{v_{\rm esc}}{\sqrt{3}} . \tag{33}$$

Figure 5 of Zappala et al. (1984) shows that the region bound by the diagonal lines representing $V_{\rm ej} = \sqrt{2}V_{\rm esc}$ and $V_{\rm ej} = V_{\rm esc}$ (the lower limit to the observed velocities) is the region in which self-gravitational effects are most important, and indeed this region is populated by many asteroid families.

Gauss's equations of motion (Brouwer & Clemence 1961; Zappala et al. 1984) can be used to relate changes in the velocity of the particle with changes in its orbital elements. Using the velocity dispersion given in equation (33), we can deduce a maximum dispersion in semimajor axis. Gauss's equations are

$$\Delta a = \frac{2}{n'\sqrt{1-e'^2}}\left[(1 + e'\cos f')\Delta v_t + e'\sin f'\Delta v_r\right] , \tag{34}$$

$$\Delta e = \frac{\sqrt{1-e'^2}}{n'a'}\left[\frac{\left(e' + 2\cos f' + e'\cos^2 f'\right)}{1 + e'\cos f'}\Delta v_t + \sin f'\Delta v_r\right] , \tag{35}$$

$$\Delta I = \frac{\sqrt{1-e'^2}}{n'a'}\left[\frac{\cos(\omega'+f')}{1+e'\cos f'}\right]\Delta v_\perp \ . \tag{36}$$

For the 3 : 2 external resonance with Neptune, $a' = 39.4$ AU and $n' = 2\pi/a'^{3/2} = 2.54 \times 10^{-2}$ yr^{-1}. To zeroth order in e', Δa can now be written as

$$\Delta a \cong R_s\left(\frac{2}{3}a'^{3/2}\sqrt{\frac{2G\rho_s}{\pi}}\right) , \tag{37}$$

where $\rho_s \cong 2$ g cm^{-3} for the Plutinos. From equation (37), we can see that Δa is a function of R_s and the semimajor axis at which the resonance is located.

The above derivation of ejection velocities is based on the methods of Zappala et al. (1984) and Cellino et al. (1999), who determined asteroidal ejection velocities based on the observational evidence of the dispersions in a, e, and I of asteroid families for the $\beta = 0$ case. For each asteroid family, Zappala et al. (1984) derived the mass and velocity distributions relative to the largest family member and calculated the ejection velocities from the dispersions in proper semimajor axis using Gauss's equations (Zappala et al. 1984; Cellino et al. 1999).

We choose to rely on these methods since current laboratory work on fragment ejection velocities suffers from the fact that the targets and projectiles are much smaller (centimeters) than the asteroids or KBOs they hope to simulate (tens to hundreds of kilometers; Cellino et al. 1999; Holsapple et al. 2003). This difference is critical because collisional processes involving small targets are dominated by material strengths while those involving large targets (i.e., asteroids or KBOs) are dominated by gravitational forces (Holsapple et al. 2003). This currently unresolved problem is evidenced by the fact that the velocities obtained in the laboratory are lower by an order of magnitude than velocities obtained by studying the Δa, Δe, and ΔI of asteroid families (Giblin 1998; Cellino et al. 1999). In addition, experimental work and models have not yet been developed that fully take into account the effects collisions have on icy bodies, which is important for the study of KBO collisions (Holsapple et al. 2003). Furthermore, we do not consider collisions between particles for the sake of simplicity. In future work, a collisional model such as that described in Gustafson et al. (1992) could be applied to the breakup of KBO source bodies.

If there is no initial dispersion in velocities, particles with $\beta = 0$ that start out in the resonance will remain in the resonance. However, if the velocity dispersion is large enough, that is, if the source body is large enough, not all of the $\beta = 0$ particles will remain in the resonance. For particles with $\beta = 0$ we can calculate the maximum source body size for which $\Delta a < \delta a'_{\max}$ by substituting equation (37) into equation (28). For the 3 : 2 mean motion resonance with Neptune, assuming $e = 0.25$ and $\delta a'_{\max} = 0.5$ AU, the maximum parent body diameter for complete trapping is $\sim$60 km. It is important to note that this value is highly dependent on our assumptions about $V_{\rm ej}$. For instance, if $V_{\rm ej} = V_{\rm esc}$, then $V_\infty = 0$ and, correspondingly, $\Delta v_t = \Delta v_r = \Delta v_\perp = 0$. Then, $\Delta a = 0$ and all of the particles would be in the resonance initially.

In this paper we assume that $V_{\rm ej} = \sqrt{2}V_{\rm esc}$, which roughly gives an estimate of the average relative velocity of the particles. We consider three different cases, that of 10 and 100 km diameter source bodies and the case in which the particles have the same orbital elements as their parent bodies. We refer to this last case as the 0 km source body case. The preceding discussion on calculating Δa applies to the $\beta = 0$ case. For cases in which β is not equal to zero, radiation pressure must also be considered and is discussed in the next section.

7. ANALYTICAL PREDICTIONS FOR TRAPPING

Micron-sized dust particles can be generated in the Kuiper Belt by the breakup of KBOs. The sizes of the source bodies and the sizes of the particles themselves determine whether the particles will become trapped in a particular resonance. For instance, particles generated from a parent body larger than $\sim$60 km in diameter will not all become trapped in the resonance, since the dispersion in initial semimajor axis (Δa) of dust particles that escape from a 60 km diameter source body will be greater than the libration width ($\delta a'_{\max}$).

Trapping is also a function of β, or particle size. For particles less than $\sim$500 μm, radiation pressure plays a significant role. In § 5 we had assumed that β was zero. However, the location of the resonance (given by eq. [38]) is a function of β, and as β increases, a' decreases:

$$a' = a'_{\beta=0}(1-\beta)^{1/3} = a_{\rm N}\left(\frac{p+q}{p}\right)^{2/3}(1-\beta)^{1/3} , \tag{38}$$

$$n' = \sqrt{\frac{GM_\odot(1-\beta)}{a'^3}} . \tag{39}$$

Shown in Table 3 is the location of the 3 : 2 external mean motion resonance as a function of β. The particle diameters in the table are obtained by assuming that the particles are spheres composed of astronomical silicate (Draine & Lee 1984). (The term "astronomical silicate" refers to a dielectric function determined by using laboratory measurements of crystalline olivine, which is constrained by infrared observations of dust grains [Draine & Lee 1984]. It is not a physical material but a simulated average of materials of

TABLE 3
LOCATION OF THE 3 : 2 EXTERNAL MEAN MOTION RESONANCE AS A FUNCTION OF β

Sphere Diameter (μm)	$\beta = \lvert\boldsymbol{F}_{\rm rad}\rvert/\lvert\boldsymbol{F}_{\rm grav}\rvert$	a'_β (AU)
4	0.12928	37.61
7	0.07104	38.43
10	0.04868	38.74
13	0.03688	38.90
20	0.02343	39.08
50	0.00905	39.27
100	0.00446	39.33
	0	39.39

NOTES.—Particle diameters are obtained by assuming that the particles are spheres composed of astronomical silicate. However, the calculations in this paper are performed as a function of β, which allows for a wider assumption of particle sizes, shapes, materials, and morphology since β is highly dependent on particle mass but less dependent on particle shape or structure (Gustafson et al. 2001).

TABLE 4
CRITICAL PARAMETERS FOR A 10 μm DIAMETER DUST PARTICLE ($\beta = 0.04868$)

p	q	$(p+q):p$	e'	α	$f_d(\alpha)$	$e'_{\rm min}$	$e'_{\rm max}$	$e'_{\rm crit}$	$P_{\rm capture}$ (%)
2	1	3:2	0.050	0.776	2.641	0.00196	0.365	0.0426	22.0
2	1	3:2	0.250	0.776	2.641	0.00196	0.365	0.0426	2.0
1	1	2:1	0.050	0.641	1.740	0.0135	0.447	0.0325	14.6
1	1	2:1	0.250	0.641	1.740	0.0135	0.447	0.0325	1.3

NOTE.—Note that for the 2:1 resonance, the indirect term of the disturbing function must be taken into account, $f_i(\alpha) = -0.5/\alpha$. The semimajor axis of Neptune, $a_{\rm N}$, is taken to be 30.06 AU, making $\alpha = 30.06/a'$.

which dust grains are composed.) The calculations in this paper are performed as a function of β, which allows for a wider assumption of particle sizes and shapes since for astronomical silicate β is highly dependent on particle mass but less dependent on particle shape or structure (Gustafson et al. 2001). Particles with a high enough value of β will get "blown out" of the maximum libration width and will not remain in resonance, at least initially. As a result of PR drag, they could eventually spiral into orbits with smaller and smaller semimajor axes until they become trapped in the resonance, or they could become trapped in the other resonances that populate the inner Kuiper Belt, such as the 2:1 or the 5:3 mean motion resonances. It is necessary to run numerical integrations to understand this complicated behavior; however, we can make some analytical predictions about it.

Neglecting all forces except PR drag, radiation pressure, and gravity, we can calculate the minimum value of the eccentricity a particle needs to have to become trapped in the 3:2 resonance, as well as the smallest size particle, corresponding to a maximum value of β, that can be trapped (Dermott et al. 1988a; Weidenshilling & Jackson 1993; Jayaraman 1995). To find the minimum eccentricity a particle must have to become trapped in an external mean motion resonance, we equate the magnitude of the change in semimajor axis with time due to resonant trapping, $da'/dt|_{\rm res}$, with the change in semimajor axis with time due to PR drag, $da'/dt|_{\rm PR}$. Neglecting terms of order e'^2 and higher and solving for e' yields

$$e'_{\rm min} \gtrsim \frac{(GM_\odot)^{1/2}}{f_d(\alpha)\mu_{\rm N} c} \frac{p^{1/3}}{(p+q)^{4/3}} \frac{\beta}{a_{\rm N}^{1/2}(1-\beta)^{2/3}} , \qquad (40)$$

where $\mu = GM_{\rm N}$. We can then solve equation (40) for β in order to determine $\beta_{\rm max}$, the maximum value of β a particle can have and still remain trapped in a given resonance. Since β is a function of particle size, $\beta_{\rm max}$ gives a limit on the smallest particles that can be trapped in resonance. Unfortunately, equation (40) cannot be easily solved for $\beta_{\rm max}$ since it is not a simple function of β and since $f_d(\alpha)$ is a function of β. Nevertheless, an approximate expression for $\beta_{\rm max}$ can be written as

$$\frac{\beta_{\rm max}}{(1-\beta_{\rm max})^{2/3}} \lesssim \frac{e' a_{\rm N}^{1/2} f_d(\alpha)\mu_{\rm N} c}{(GM_\odot)^{1/2}} \frac{(p+q)^{4/3}}{p^{1/3}} . \qquad (41)$$

For $e' = 0.05$, $0.13 \lesssim \beta_{\rm max} \lesssim 0.64$, which corresponds to a particle diameter, d, of roughly 1 $\mu{\rm m} \lesssim d \lesssim 4$ μm assuming a spherical particle composed of astronomical silicate. $\beta_{\rm max}$ is somewhat challenging to calculate since the right-hand side of equation (41) is also a function of $\beta_{\rm max}$, since α and $f_d(\alpha)$ are functions of β. Another value of interest is the maximum value of eccentricity, $e'_{\rm max}$, a particle can have in a given resonance. As derived in Weidenshilling & Jackson (1993), this maximum value is given as

$$e'_{\rm max} = \sqrt{\frac{2}{5(p+q)}} , \qquad (42)$$

neglecting terms higher than order e'^2. The derivation is based on analysis of the evolution of the eccentricity as a function of time but will not be discussed in this paper. Values for $e'_{\rm min}$ and $e'_{\rm max}$ are given in Tables 4 and 5 as a function of p, q, and β. Two other important quantities remain to be discussed, the critical value of the eccentricity for particles moving into the resonance from exterior orbits, $e'_{\rm crit}$, and the capture probability, $P_{\rm capture}$. For a first-order resonance ($q = 1$), the critical value of eccentricity is given as

$$e'_{\rm crit} = \left[\frac{2\sqrt{6}(M_{\rm N}/M_\odot)\alpha^3 f_d(\alpha)}{p^2}\right]^{1/3} , \qquad (43)$$

TABLE 5
CRITICAL PARAMETERS FOR A 100 μm DIAMETER DUST PARTICLE ($\beta = 0.00446$)

p	q	$(p+q):p$	e'	α	$f_d(\alpha)$	$e'_{\rm min}$	$e'_{\rm max}$	$e'_{\rm crit}$	$P_{\rm capture}$ (%)
2	1	3:2	0.050	0.764	2.497	0.000184	0.365	0.0412	20.898
2	1	3:2	0.250	0.764	2.497	0.000184	0.365	0.0412	1.869
1	1	2:1	0.050	0.631	1.693	0.00144	0.447	0.0302	13.107
1	1	2:1	0.250	0.631	1.693	0.00144	0.447	0.0302	1.172

NOTES.—Note that for the 2:1 resonance, the indirect term of the disturbing function must be taken into account, $f_i(\alpha) = -0.5/\alpha$. The semimajor axis of Neptune, $a_{\rm N}$, is taken to be 30.06 AU, making $\alpha = 30.06/a'$.

where we have assumed that the mass of the dust particle is zero (Dermott et al. 1988a). The probability of capture into a first-order resonance, $P_{\rm capture}$, can be determined from $e'_{\rm crit}$. From Dermott et al. (1988a),

$$P_{\rm capture} = \begin{cases} 1 & \text{for } e' < e'_{\rm crit} , \\ \dfrac{2}{\pi 3^{3/4}} \left(\dfrac{e'_{\rm crit}}{e'} \right)^{3/2} & \text{for } e' \gg e'_{\rm crit} , \end{cases} \quad (44)$$

and is presented in Tables 4 and 5. It should be noted that the equations for $e'_{\rm crit}$ and $P_{\rm capture}$ are applicable only under the adiabatic criterion, which states that the change in semimajor axis due to drag (in this case, PR drag) in one libration period should be much less than $\delta a'_{\rm max}$, the resonant libration width:

$$\frac{da'}{dt}|_{\rm PR} T_{\rm lib} \ll \delta a'_{\rm max} . \quad (45)$$

As discussed in Dermott et al. (1988a), the adiabatic criterion is valid only for well-separated resonances. To determine whether the Kuiper disk is in the adiabatic region, we chose $T_{\rm lib} = 19,670$ yr, the libration period of Pluto, since the pendulum model does not provide accurate values for the libration period for the 3 : 2 resonance with Neptune. Using equation (26) and rewriting equation (3) in terms of the primed quantities, for an eccentricity $e' = 0.25$ and $\beta = 0.04868$ (for a 10 μm diameter spherical particle), $da'/dt|_{\rm PR} = 1.89 \times 10^{-6}$ AU yr^{-1} and $\delta a'_{\rm max} \approx 0.52$ AU, so that $da'/dt|_{\rm PR} T_{\rm lib} = 0.037$ AU, which is, indeed, much less than the libration width of 0.52 AU, and therefore dust particles in the 3 : 2 mean motion resonance with Neptune are in the adiabatic regime.

In the preceding discussion we have neglected all forces except radiation pressure, gravity, and PR drag. However, other forces such as the Lorentz force and the effect of neutral interstellar gas drag are important to Kuiper dust grains. For instance, Lorentz forces become important for small particles at large heliocentric distances since the Lorentz force varies as $1/r$ while gravity and radiation pressure vary as $1/r^2$ (Gustafson 1994). These additional forces are not incorporated in the theory, so instead they must be included in numerical simulations.

Tables 4 and 5 also list some parameters for the 2 : 1 resonance. The 2 : 1 resonance is a special case of an external resonance since when $p = 1$, the indirect term of the expansion of the disturbing function, $f_i(\alpha)$, must be taken into account. Taking into account the extra factor of α in front of $f_d(\alpha)$ for external resonances in equation (24), equation (27) can now be written as

$$C'_r = \left(\frac{GM_{\rm N}}{a'^2 a_{\rm N} n'} \right) \left[f_d(\alpha) + \frac{f_i(\alpha)}{\alpha} \right] , \quad (46)$$

where $f_i(\alpha) = -1/(2\alpha)$. This in turn can be used to calculate the libration width for the 2 : 1 resonance. Following Murray & Dermott (1999), we calculate the libration widths for the 5 : 3 and 6 : 4 resonances. Since they are second-order resonances, the shapes of their libration widths are different than those of the 2 : 1 and 3 : 2 resonances.

8. NUMERICAL INTEGRATIONS

We use the numerical integrator RADAU (Everhart 1989) to find the percentages of particles in resonance for a variety of initial conditions. RADAU is a very accurate integration code that employs the Runge-Kutta method with Gauss-Radau spacings. RADAU is very flexible, allowing the introduction of additional forces. Most of the runs in this paper have 249 particles. The error in the estimate of the percentage of particles in resonance is $100\sqrt{N_r}/N_r$ percent, where N_r is the number of particles in resonance. (However, when N_r is zero, we do not give an error estimate.) In order to decrease the error, we increase the total number of particles to 1017 for a small number of runs. The integrations were run for 250,000 yr and the orbital elements of the particles were output every 100 yr so we could obtain an accurate variation of the resonant argument. The integrator considers PR drag, solar wind drag, radiation pressure, and the effects of the gravitational perturbations of seven planets. Mercury and Pluto are excluded from consideration since their masses are very low. In addition, in some of the runs, we have considered the effect of the Lorentz force on the particles, as well as the effect of neutral interstellar gas drag. Runs have been completed for particles ejected from source bodies of 0, 10, and 100 km with a variety of sizes: 4, 10, 20, 50, and 100 μm diameter spherical astronomical silicate particles (corresponding to $\beta = 0.12928$, 0.04868, 0.02343, 0.00905, and 0.00446) and the $\beta = 0$ or no drag case. We also run several cases for particles having $\beta = 0.07104$ and 0.03688, corresponding to 7 and 13 μm spherical particles composed of astronomical silicate. We find that as β increases, the percentage of particles in the 3 : 2 mean motion resonance decreases.

Shown in Figures 5 and 6 is an example of a particle that is in the 3 : 2 mean motion resonance with Neptune for the entire length of the integration. The eccentricity versus semimajor axis for particle 1 is plotted in Figure 5. The run consists of 249 particles integrated for 250,000 yr and includes the effects of the gravitational perturbations of

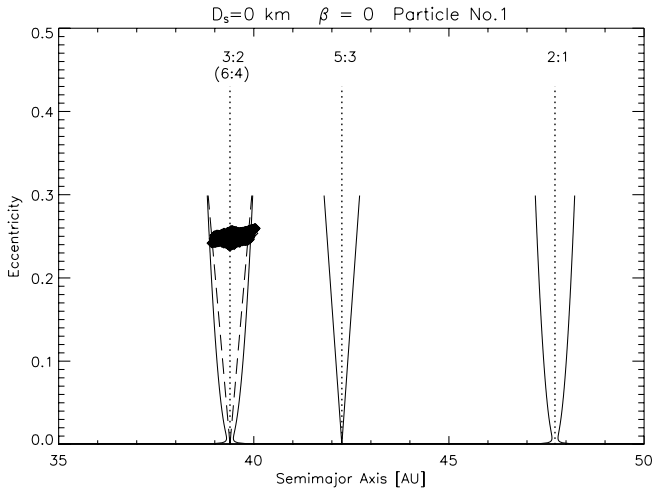

FIG. 5.—Eccentricity vs. semimajor axis for particle 1 in a RADAU run for the no drag case ($\beta = 0$) including the effects of the gravitational perturbations of seven planets. Mercury and Pluto are excluded. The run consists of 249 particles integrated for 250,000 yr. The particles, having β equal to zero, were released from a 0 km source body in a Pluto-like orbit. Each diamond represents the particle's orbital elements at 100 yr intervals. The 3 : 2, 5 : 3, and 2 : 1 libration widths are shown as solid lines, while the 6 : 4 libration width is shown as a dashed line. The exact location for each resonance is plotted as a dotted line. It is clear that particle 1 is trapped in the 3 : 2 mean motion resonance with Neptune, since for the majority of the time the particle stays within the 3 : 2 libration width. In Fig. 6 it becomes apparent that particle 1 is indeed trapped in the 3 : 2 resonance for the entire 250,000 yr. None of the particles in this run were excluded from the system.

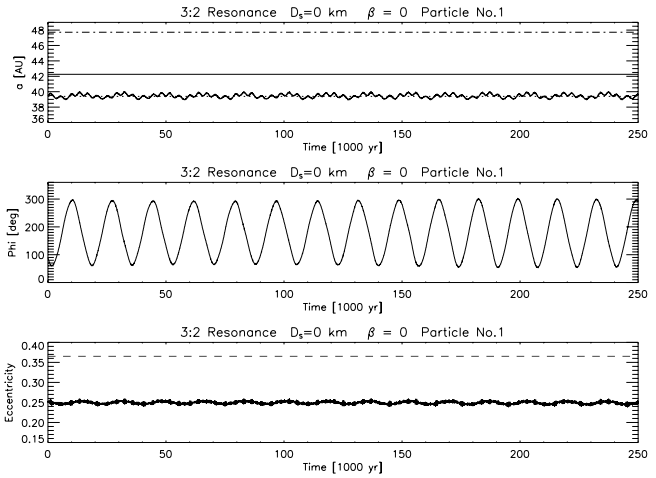

FIG. 6.—Variation of semimajor axis, resonant argument, and eccentricity with time for particle 1 in a RADAU run for the no drag case ($\beta = 0$) including the gravitational effects of seven planets. Mercury and Pluto are excluded. The run consists of 249 particles integrated for 250,000 yr. The particles, having β equal to zero, were released from a 0 km source body in a Pluto-like orbit. *Top:* Variation of semimajor axis, a, with time. The exact location for the 3 : 2 resonance for the $\beta = 0$ case is plotted as a dotted line. The exact locations of the 5 : 3 and 2 : 1 resonances are plotted as a solid line and a dot-dashed line, respectively. The semimajor axis of particle 1 is clearly librating around the exact location of the 3 : 2 resonance. *Middle:* Variation of the resonant argument for the 3 : 2 resonance (where $j_1 = 3$, $j_2 = -2$, $j_3 = -1$, $j_4 = 0$, $j_5 = 0$, and $j_6 = 0$) with time. The resonant argument is librating the entire time, showing that the particle is trapped in the 3 : 2 resonance for the entire integration time of 250,000 yr. *Bottom:* Variation of the eccentricity with time for particle 1. The dashed line is the value of $e_{\max}$, the maximum value of eccentricity a particle trapped in the 3 : 2 resonance can reach. As expected, the particle's eccentricity never reaches $e_{\max}$ in this no drag case.

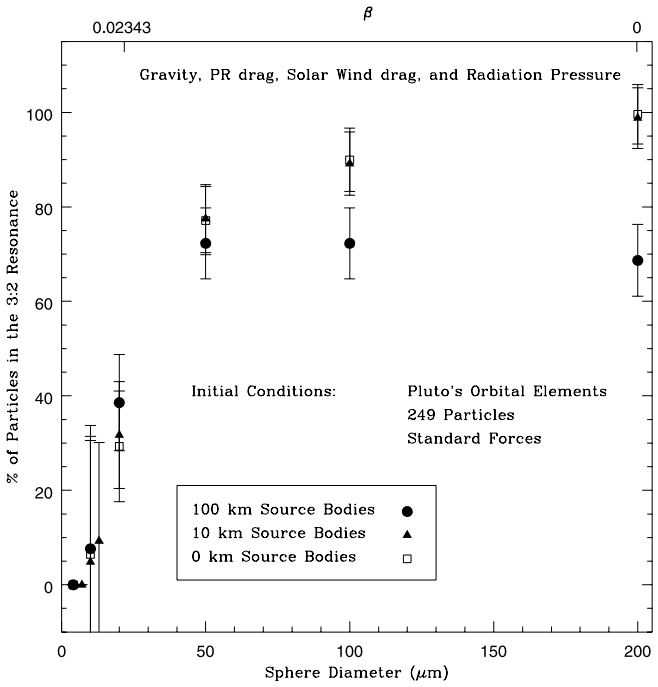

FIG. 7.—Percentage of particles in the 3 : 2 mean motion resonance with Neptune for the case including the effects of gravity, PR drag, solar wind corpuscular drag, and radiation pressure, as a function of β (particle size). The open squares correspond to the case in which the particles had no initial velocity dispersion, while the filled triangles and filled circles correspond to the cases in which the particles were generated from 10 and 100 km diameter source bodies, respectively. The particles were integrated for 250,000 yr. Each numerical run is composed of 249 particles, giving an error in the estimate of the percentage of particles in resonance of $\sim 100\sqrt{N_r}/N_r$ percent, where N_r is the number of particles in resonance. For the case in which $N_r = 0$, we do not give an error estimate. [*See the electronic edition of the Journal for a color version of this figure*.]

seven planets. The particles, having β equal to zero, were released from a 0 km source body in a Pluto-like orbit. Each diamond represents the particle's orbital elements at 100 yr intervals. The 3 : 2, 5 : 3, and 2 : 1 maximum libration widths are shown as solid lines, while the 6 : 4 maximum libration width is shown as a dashed line. The exact location for each resonance is plotted as a dotted line. It appears that particle 1 is trapped in the 3 : 2 mean motion resonance with Neptune, since for the majority of the time the particle stays within the 3 : 2 libration width. In Figure 6 it becomes apparent that particle 1 is indeed trapped in the 3 : 2 resonance for the entire 250,000 yr since the resonant argument, φ, is clearly librating as opposed to circulating. Figure 6 shows the variation of semimajor axis, resonant argument, and eccentricity with time for particle 1 in the aforementioned RADAU run. The exact location for 3 : 2 resonance for the no drag ($\beta = 0$) case is plotted as a dotted line. The semimajor axis of particle 1 is clearly librating around the exact location of the 3 : 2 resonance. The resonant argument, φ, is very clearly librating, showing that the particle is trapped in the 3 : 2 resonance for the entire integration time of 250,000 yr. Also plotted is the variation of the eccentricity with time. The dashed line is the value of $e_{\max}$, the maximum value of eccentricity a particle trapped in the 3 : 2 resonance can reach. As expected, the particle's eccentricity never reaches $e_{\max}$ for the no drag case.

8.1. *Results for the Standard Forces Case*

The percentage of particles in the 3 : 2 mean motion resonance with Neptune for the case including the effects of gravity, PR drag, solar wind corpuscular drag, and radiation pressure as a function of β (particle size) is shown in Figure 7. The open squares correspond to the case in which the particles had no initial velocity dispersion, while the filled triangles and filled circles correspond to the cases in which the particles were generated from 10 and 100 km diameter source bodies, respectively. The particles were integrated for 250,000 yr. Each numerical run is composed of 249 particles.

0 km *diameter source bodies*.—For the runs generated with no velocity dispersion, the percentage of particles that remain in (or are later recaptured into) the 3 : 2 mean motion resonance roughly increases with decreasing β (i.e., increasing particle size). Numerical runs were performed for the no drag case and cases with β-values of 0.12928, 0.04868, 0.02343, 0.00905, and 0.00446 (corresponding to spheres with diameters of 4, 10, 20, 50, and 100 μm). The large error bars for the smaller particle sizes (higher β-values) are due to the lower percentage of particles trapped for those cases, since we are assuming Poisson statistics. However, a trend is evident, with no particles in resonance for the 4 μm case while nearly all (99.6%) of the particles are in resonance for the $\beta = 0$ case. This is in agreement with the value of $\beta_{\max}$ of $\sim$0.13 (corresponding to a 4 μm diameter spherical particle) calculated using equation (41).

10 km *diameter source bodies*.—The runs with particles generated from 10 km diameter source bodies also exhibit the trend that the percentage of particles that remain in (or

are later recaptured into) the 3 : 2 mean motion resonance roughly increases with decreasing β. Numerical runs were performed for the no drag case and cases with β-values of 0.12928, 0.07104, 0.04868, 0.03688, 0.02343, 0.00905, and 0.00446 (corresponding to spheres with diameters of 4, 7, 10, 13, 20, 50, and 100 μm). The large error bars for the smaller particle sizes (higher β-values) are due to the lower percentage of particles trapped for those cases, but a trend is still evident, with no particles in resonance for either the 4 or 7 μm cases while nearly all (98.8%) of the particles are in resonance for the $\beta = 0$ case.

100 km *diameter source bodies*.—The runs with particles generated from 100 km diameter source bodies were performed for the no drag case and cases with β-values of 0.12928, 0.04868, 0.02343, 0.00905, and 0.00446 (corresponding to spheres with diameters of 4, 10, 20, 50, and 100 μm). For sphere sizes up to 50 μm, the percentage of particles in the 3 : 2 resonance roughly increases with increasing particle size. However, the percentage of particles in resonance levels off at a value of $\sim$71% for particle sizes $\geq$50 μm ($\beta \leq$ 0.00905). This is in agreement with the analytical prediction given in § 7 that particles generated from a parent body larger than $\sim$60 km in diameter will not all become trapped in the resonance, since the dispersion in initial semimajor axis of dust particles that escape from a 60 km diameter source body will be greater than the libration width.

The percentage of 10 μm diameter particles trapped in the 3 : 2 resonance for different sized source bodies (6.4%, 4.8%, and 7.6% for 0, 10, and 100 km source bodies, respectively) falls within the predicted values of $P_{\rm capture}$ listed in Tables 4 and 5: $2.0\% < P_{\rm capture} < 22.0\%$. However, in the case of the 100 μm diameter particles, significantly more particles are trapped than are predicted by $P_{\rm capture}$ (90.0%, 89.2%, and 72.3% for 0, 10, and 100 km source bodies, respectively) compared to $1.9\% < P_{\rm capture} < 20.9\%$. Our capture probabilities are larger than predicted values for the 100 μm diameter particles because our particles started out within the libration width and did not need to first evolve into the resonance, making capture into resonance for large particles much easier.

Plotted in Figure 8 is the X-Y distribution of orbits for the standard forces case in the rotating frame for the case of 7 (Figs. 8*a* and 8*b*) and 50 μm diameter particles (Figs. 8*c* and 8*d*), and the $\beta = 0$ case (Figs. 8*e* and 8*f*) assuming that the particles originate from 10 km diameter source bodies. The plots on the left are in terms of brightness, while those on the right are number density plots for one individual particle. None of the 7 μm particles were trapped in the 3 : 2 resonance, and correspondingly Figure 8*b* shows that particle 2 is not in resonance. Figures 8*d* and 8*f* show an example of a 50 μm particle and a $\beta = 0$ particle in resonance, respectively. Note the depletion of particles near Neptune (represented by a large square) since particles in resonance with Neptune avoid the planet. Figure 8*e* also shows a depletion in particles near Neptune. However, this effect becomes less noticeable when there are a significant number of particles that are not in resonance as shown in Figure 8*c*. For the $\beta = 0$ case, 98.8% of the particles are in resonance for an average of approximately 220,000 yr, so the effect is noticeable and can be compared to Figures 1 and 2, keeping in mind that a depletion in number density will produce a dimmer section of the disk. As seen in Figure

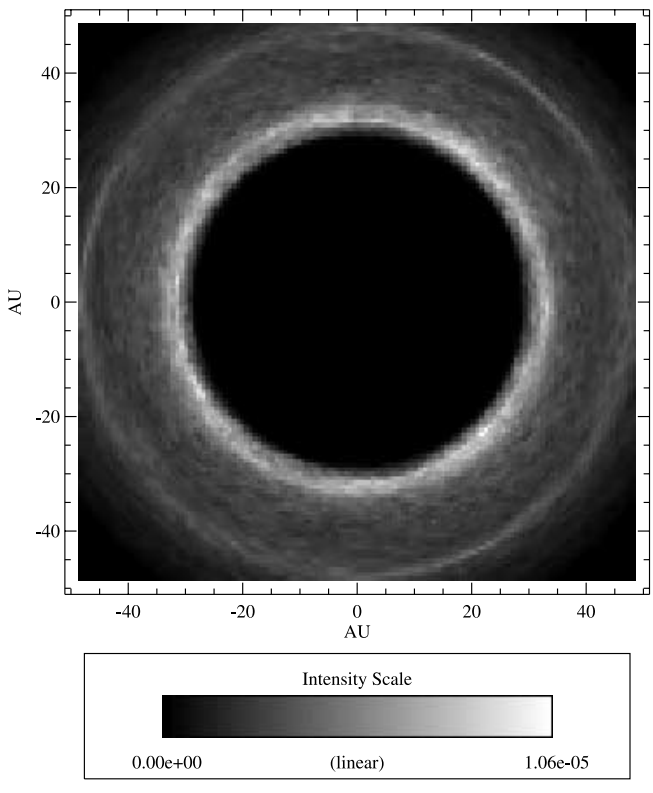

FIG. 8*a*

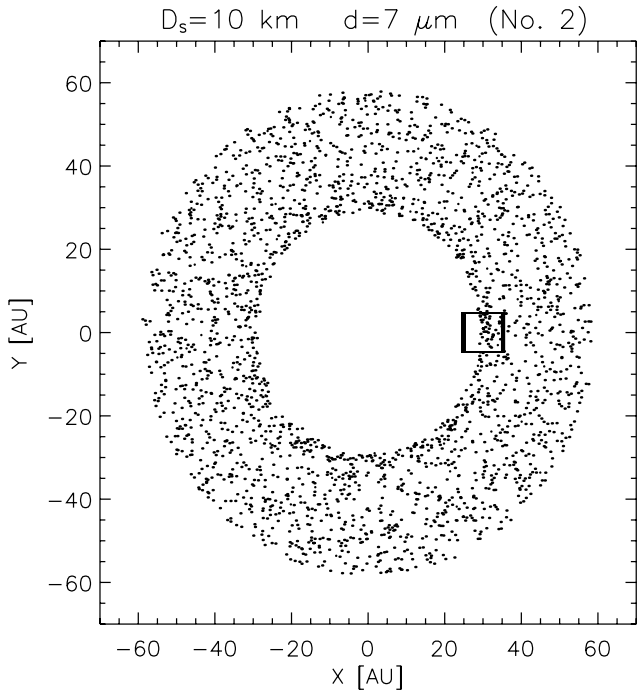

FIG. 8*b*

FIG. 8.—X-Y distribution of orbits for the standard forces case in the rotating frame in terms of (*left*) brightness and (*right*) number density for a specific particle. The location of Neptune is represented by a large square. [*See the electronic edition of the Journal for a color version of Figs. 8a, 8c, and 8e*.]

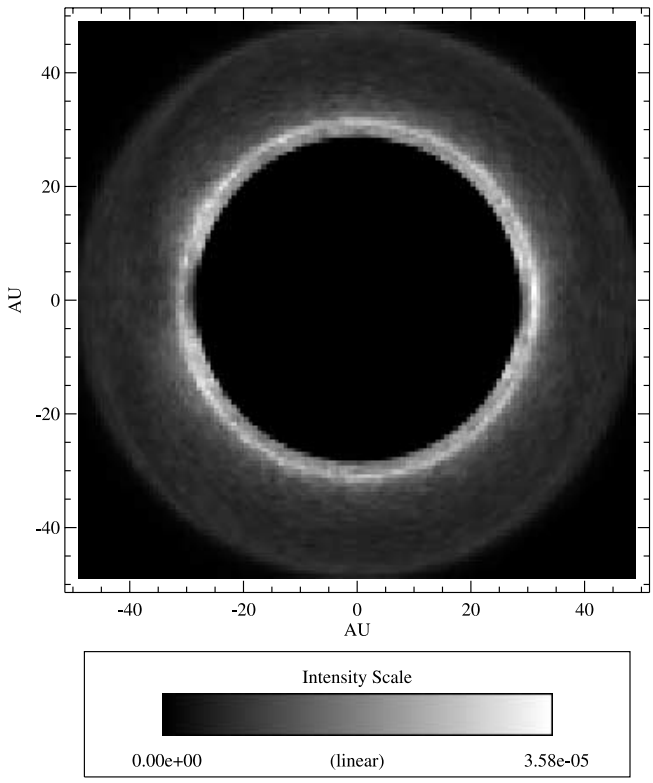

FIG. 8*c*

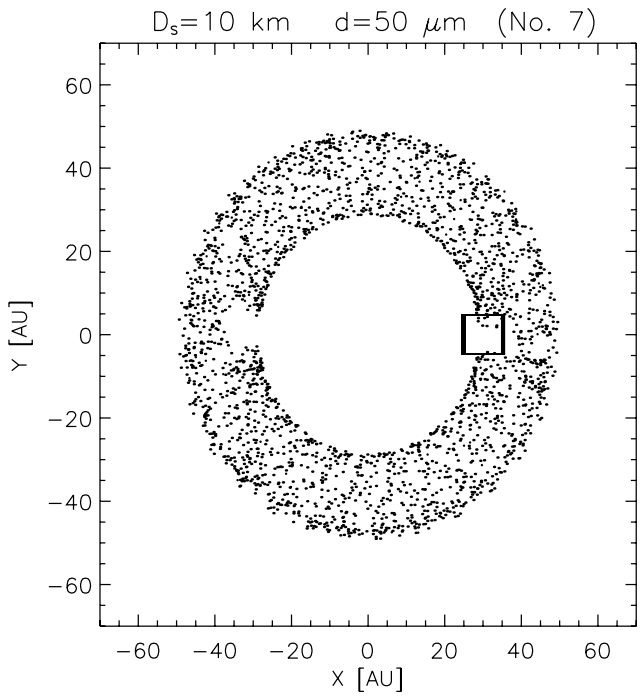

FIG. 8*d*

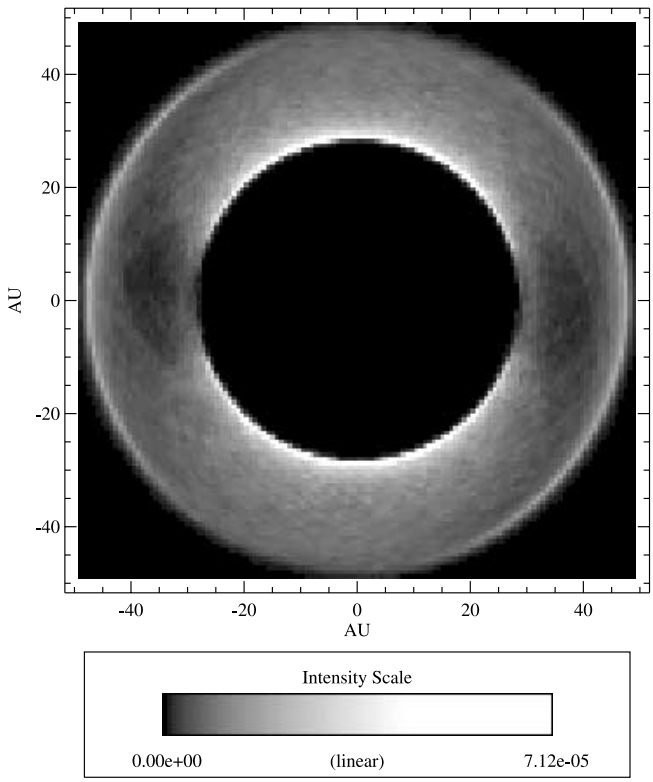

FIG. 8*e*

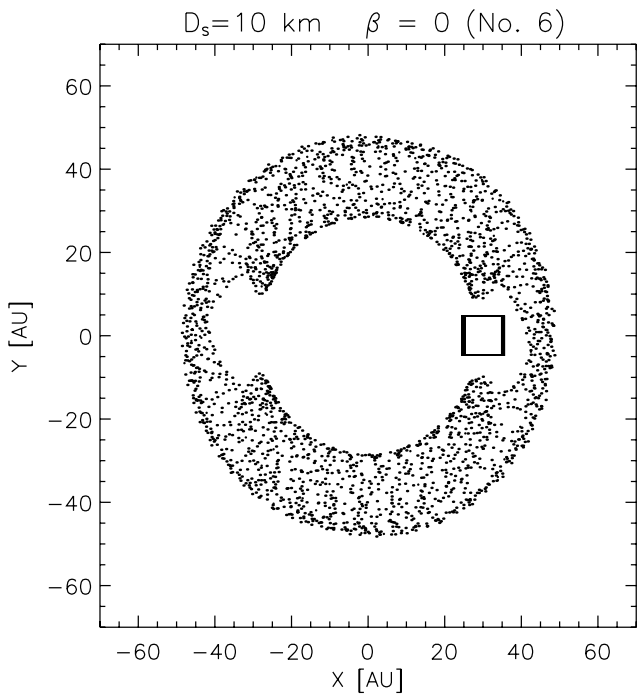

FIG. 8*f*

8*c*, for the 50 μm case, the effect is not as noticeable because only 77.5% of the particles are in resonance and they are in resonance for an average of 130,000 yr. However, there is a gap in brightness opposite the location of Neptune. There are no 7 μm particles in the 3 : 2 resonance so there is no depletion of particles near Neptune in either Figure 8*a* or Figure 8*b*. As a result of radiation pressure, the 7 μm particle disk has a larger radial extent. In addition, there is a bright ring of material at approximately 45 AU that could be due to particles being trapped in other resonances, such as the 2 : 1 resonance.

In the preceding runs, we have included gravity, radiation pressure, solar wind corpuscular drag, and PR drag. However, other forces, such as the Lorentz force and the effect of neutral interstellar gas drag, could potentially be important for dust grains in the Kuiper disk. Our goal is to determine whether the addition of these two effects will have an impact on the percentage of particles in the 3 : 2 resonance. The Lorentz force has been included in the next set of runs that will be discussed.

8.2. *The Lorentz Force*

Our goal is to determine whether the addition of the Lorentz force will have an impact on the percentage of particles in the 3 : 2 resonance. As discussed previously, interplanetary dust particles are charged and a typical particle is expected to have a net positive potential, U, of approximately 5 V (Goertz 1989; Gustafson 1994). However, this quantity is uncertain and could be as high as 100 V (Leinert & Grün 1990). We have made a set of runs including the Lorentz force with $U = 5$ V that are identical to those presented in Figure 7. In addition, since U is uncertain, we have included some runs with $U = 20$ V.

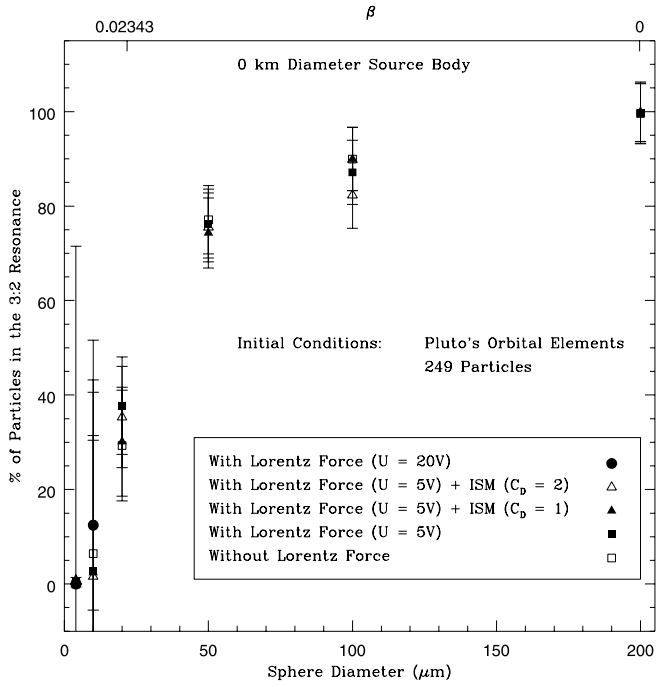

FIG. 9.—Percentage of particles in the 3 : 2 mean motion resonance with Neptune, assuming that particles were generated from a source body of 0 km in diameter (i.e., with no initial velocity dispersion) in the 3 : 2 resonance, as a function of β. The open squares correspond to RADAU runs with the effects of gravity, PR drag, solar wind corpuscular drag, and radiation pressure included, that is, the standard forces. The filled squares and filled circles correspond to RADAU runs that include, in addition to the standard forces, the Lorentz force with a potential U equal to 5 and 20 V, respectively. The filled and open triangles correspond to runs that include the standard forces, the Lorentz force with $U = 5$ V, and the effects of neutral interstellar gas drag assuming that C_D is equal to 1 and 2, respectively. Each numerical run is composed of 249 particles, giving an error in the estimate of the number of particles in resonance of $\sim 100\sqrt{N_r}/N_r$ percent, where N_r is the number of particles in resonance. The particles were integrated for 250,000 yr. [*See the electronic edition of the Journal for a color version of this figure.*]

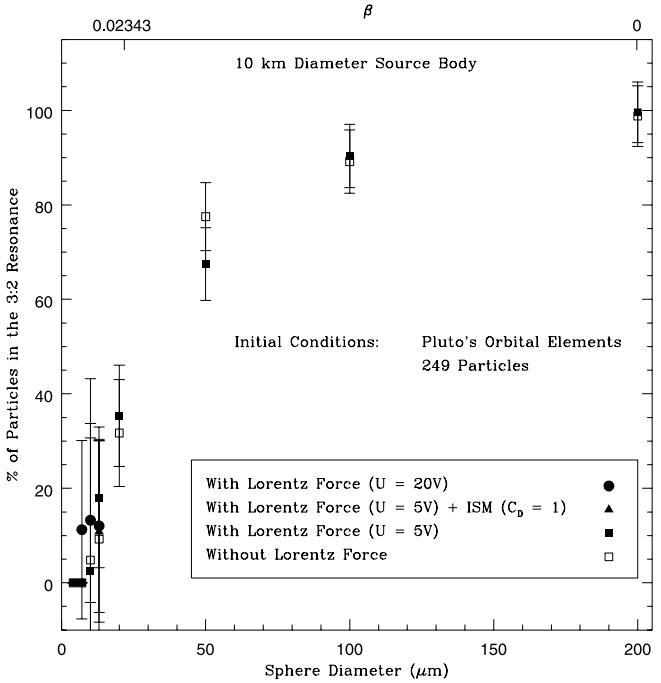

FIG. 10.—Percentage of particles in the 3 : 2 mean motion resonance with Neptune, assuming that particles were generated from a source body of 10 km in diameter, as a function of β. The open squares correspond to RADAU runs including the standard forces, that is, the effects of gravity, PR drag, solar wind corpuscular drag, and radiation pressure. The filled squares and filled circles correspond to RADAU runs that include, in addition to the standard forces, the Lorentz force with a potential, U, equal to 5 and 20 V, respectively. The filled triangles correspond to RADAU runs that include the standard forces, the Lorentz force with $U = 5$ V, and the effects of neutral interstellar gas drag assuming $C_D = 1$. Each numerical run is composed of 249 particles, giving an error in the estimate of the number of particles in resonance of $\sim 100\sqrt{N_r}/N_r$ percent, where N_r is the number of particles in resonance. The particles were released from 10 km diameter source bodies in Pluto-like orbits and were integrated for 250,000 yr. [*See the electronic edition of the Journal for a color version of this figure.*]

The results of the integrations are shown in Figures 9, 10, and 11 for particles generated from 0 (i.e., no velocity dispersion), 10, and 100 km diameter source bodies, respectively. Plotted are the percentages of particles in the 3 : 2 mean motion resonance with Neptune versus β, which is also translated to particle diameter assuming that particles are spheres composed of astronomical silicate (see Table 3). The open squares correspond to RADAU runs including the "standard forces," that is, the effects of gravity, PR drag, solar wind corpuscular drag, and radiation pressure (or in the $\beta = 0$ case, only gravity). The filled squares and filled circles correspond to RADAU runs that also include the Lorentz force with a potential, U, equal to 5 and 20 V, respectively. The triangles correspond to RADAU runs that include the standard forces, the Lorentz force with $U = 5$ V, and the effects of neutral interstellar gas drag assuming that C_D is equal to 1 (*filled triangles*) or $C_D = 2$ (*open triangles*), which is discussed in a later section. Each numerical run shown in Figures 9, 10, and 11 is composed of 249 particles.

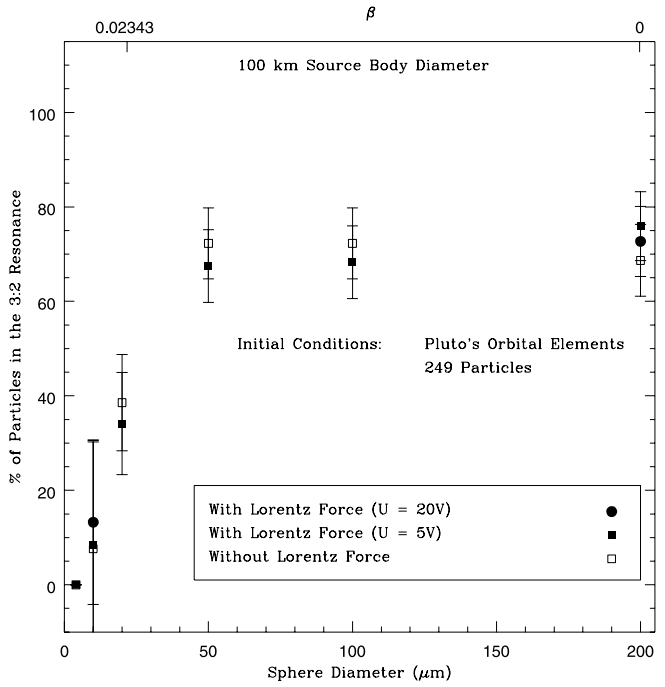

FIG. 11.—Percentage of particles in the 3 : 2 mean motion resonance with Neptune, assuming that particles were generated from a source body of 100 km in diameter, as a function of β. The open squares correspond to RADAU runs including the standard forces, that is, the effects of gravity, PR drag, solar wind corpuscular drag, and radiation pressure. The filled squares and filled circles correspond to RADAU runs that include, in addition to the standard forces, the Lorentz force with a potential, U, equal to 5 and 20 V, respectively. Each numerical run is composed of 249 particles, giving an error in the estimate of the number of particles in resonance of $\sim 100\sqrt{N_r}/N_r$ percent, where N_r is the number of particles in resonance. The particles were released from 100 km diameter source bodies in Pluto-like orbits and were integrated for 250,000 yr. [*See the electronic edition of the Journal for a color version of this figure.*]

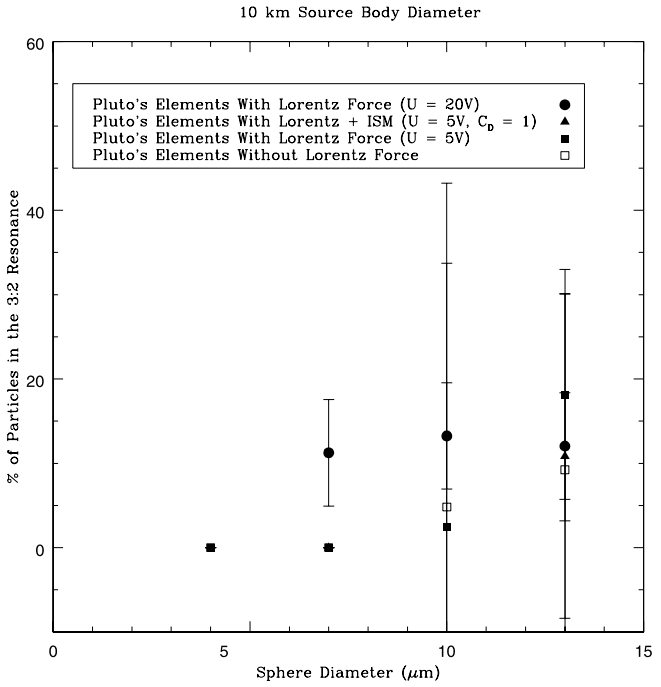

FIG. 12.—Close-up of the plot of the percentage of particles in the 3 : 2 mean motion resonance with Neptune assuming that particles were generated from a source body of 10 km in diameter in the 3 : 2 resonance. The open squares correspond to RADAU runs including the standard forces, that is, the effects of gravity, PR drag, solar wind corpuscular drag, and radiation pressure. The filled squares and filled circles correspond to RADAU runs that include, in addition to the standard forces, the Lorentz force with a potential, U, equal to 5 and 20 V, respectively. The filled triangles correspond to RADAU runs that include the standard forces, the Lorentz force with $U = 5$ V, and the effects of neutral interstellar gas drag assuming $C_D = 1$. Each numerical run is composed of 249 particles, giving an error in the estimate of the number of particles in resonance of $\sim 100\sqrt{N_r}/N_r$ percent, where N_r is the number of particles in resonance. The particles were released from 10 km diameter source bodies in Pluto-like orbits and were integrated for 250,000 yr. [*See the electronic edition of the Journal for a color version of this figure.*]

As seen in Figures 9, 10, and 11, the addition of the Lorentz force with $U = 5$ V does not in general have a significant effect on whether the particles remain in the 3 : 2 resonance. However, as shown in Figure 12 and Table 6, for small particles (≈ 10 μm in diameter), the Lorentz force can have an appreciable effect especially if U is increased to 20 V. This potential is probably too high for grains in the Kuiper Belt, but it does serve as an interesting test case for the effects of the Lorentz force. Table 6 shows the trapping results for four different mean motion resonances with Neptune (3 : 2, 6 : 4, 5 : 3, and 2 : 1) with the initial conditions that the particles escaped from a source body 10 km in diameter and there are 249 particles in each run. The results appear to be counterintuitive in that more particles are trapped into the 3 : 2 resonance in the $U = 20$ V Lorentz force case than in the case without the Lorentz force. In the case of increased drag, one would expect that less particles would be trapped. However, the increase in trapping in the 3 : 2 resonance occurs because the particles in the non–Lorentz force case are getting trapped in the 5 : 3 resonance before their orbits can evolve down to a semimajor axis where they can become trapped in the 3 : 2 resonance, an

TABLE 6

A COMPARISON OF RESULTS FOR NUMERICAL RUNS (CONSISTING OF 249 PARTICLES EACH) FOR 7 μm DIAMETER PARTICLES ($\beta = 0.07104$) ORIGINATING FROM 10 km DIAMETER SOURCE BODIES

NUMERICAL RUN	PERCENTAGE OF PARTICLES TRAPPED IN RESONANCE (%)				PERCENTAGE EXCLUDED FROM SYSTEM (%)
	3 : 2	6 : 4	5 : 3	2 : 1	
Standard forces	0.0	0.0	34.1	2.4	0.0
Standard forces and Lorentz force ($U = 5$ V)	0.0	0.0	21.7	0.4	0.0
Standard forces and Lorentz force ($U = 5$ V) and ISM ($C_D = 1$)	0.0	0.0	29.3	0.4	0.0
Standard forces and Lorentz force ($U = 20$ V)	11.2	0.4	9.6	12.9	57.4

NOTES.—The error in the estimate of the percentage of particles in resonance is $100\sqrt{N_r}/N_r$ percent, where N_r is the number of particles in resonance. (However, when $N_r \approx 0$, we do not give an error estimate.)

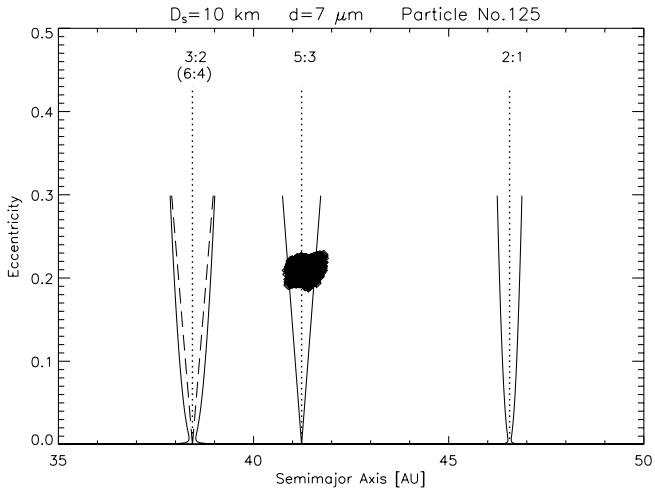

FIG. 13.—Eccentricity vs. semimajor axis for a particle trapped in the 5 : 3 mean motion resonance with Neptune. Particle 125 is from a RADAU run for the case of 7 μm diameter particles ($\beta = 0.07104$) that are released from a 10 km diameter source body. The run consists of 249 particles integrated for 250,000 yr and includes the effects of gravity, PR drag, solar wind corpuscular drag, and radiation pressure. Each diamond represents the particle's orbital elements at 100 yr intervals. The 3 : 2, 5 : 3, and 2 : 1 libration widths are shown as solid lines, while the 6 : 4 libration width is shown as a dashed line. The exact location for each resonance is plotted as a dotted line.

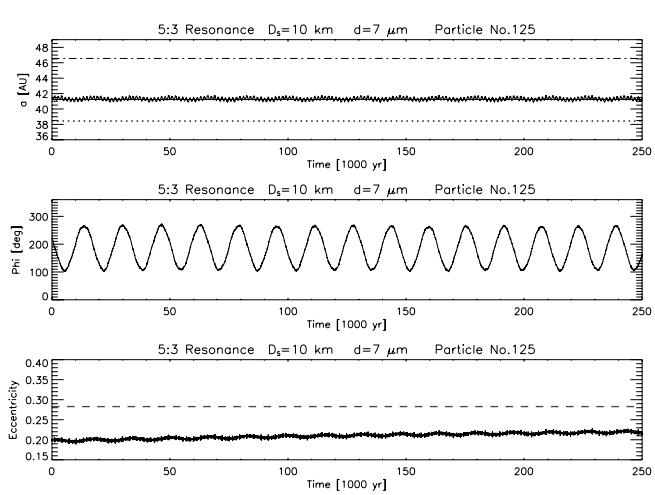

FIG. 14.—Variation of semimajor axis, resonant argument, and eccentricity with time for particle 125 in a RADAU run (for 7 μm diameter particles released from a 10 km source body) including the standard forces. The run consists of 249 particles integrated for 250,000 yr and includes the effects of gravity, PR drag, solar wind corpuscular drag, and radiation pressure. *Top:* Variation of semimajor axis, a, with time. The exact location for the 3 : 2 resonance for the $\beta = 0$ case is plotted as a dotted line. The exact locations of the 5 : 3 and 2 : 1 resonances are plotted as a solid line and a dot-dashed line, respectively. The semimajor axis of particle 125 is clearly librating around the exact location of the 5 : 3 resonance for the entire time. *Middle:* Variation of the resonant argument for the 5 : 3 resonance (where $j_1 = 5, j_2 = -3, j_3 = -2, j_4 = 0, j_5 = 0$, and $j_6 = 0$) with time. The resonant argument, φ, is clearly librating. *Bottom:* Variation of the eccentricity with time for particle 125. The dashed line is the value of $e_{\max}$, the maximum value of eccentricity a particle trapped in the 3 : 2 resonance can reach. The particle's eccentricity never reaches $e_{\max}$, nor does it appear to be approaching $e_{\max}$, implying that the particle may be trapped in the 5 : 3 resonance for much longer than 250,000 yr.

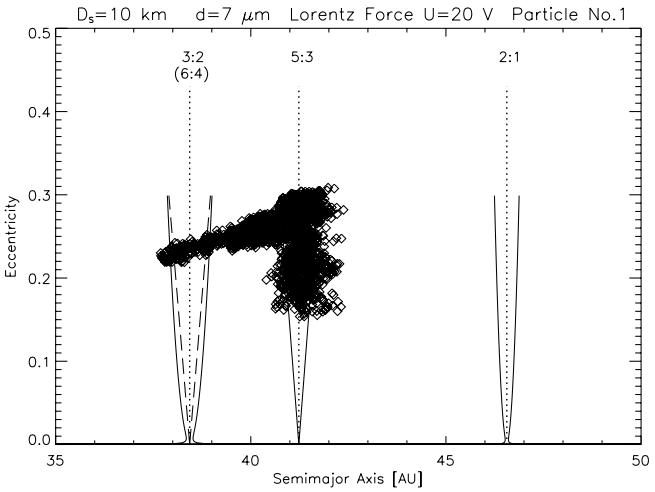

FIG. 15.—Eccentricity vs. semimajor axis for particle 1 in a RADAU run including the Lorentz force where $U = 20$ V. The $\beta = 0.07104$ (7 μm diameter) particles in this RADAU run were released from a 10 km source body. The 3 : 2, 5 : 3, and 2 : 1 libration widths are shown as solid lines, while the 6 : 4 libration width is shown as a dashed line. The exact location for each resonance is plotted as a dotted line. Each diamond represents the particle's orbital elements at 100 yr intervals. Note that for the majority of the time, particle 1 appears to be within the 5 : 3 libration width, but for a short period of time, the particle is also within both the 3 : 2 and 6 : 4 resonant widths. As can be seen in the next figure, the particle is in fact trapped in both the 5 : 3 and 3 : 2 resonances.

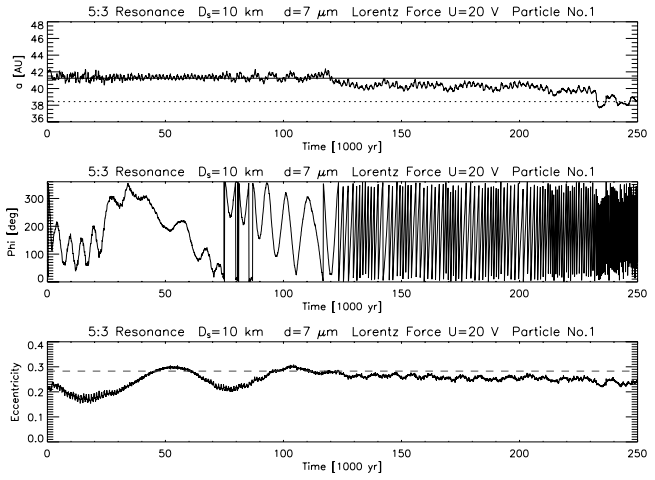

FIG. 16.—Variation of semimajor axis, resonant argument, and eccentricity with time for particle 1 in a RADAU run including the Lorentz force where $U = 20$ V. The $\beta = 0.07104$ (7 μm diameter) particles in this RADAU run were released from a 10 km source body. *Top:* Variation of semimajor axis, a, with time. The exact location for the 5 : 3 resonance is plotted as a solid line, while the exact location of the 3 : 2 resonance is plotted as a dotted line. *Middle:* Variation of the resonant argument for the 5 : 3 resonance (where $j_1 = 5, j_2 = -3, j_3 = -2, j_4 = 0, j_5 = 0$, and $j_6 = 0$) with time. For approximately the first 120,000 yr, the resonant argument is librating and therefore the particle is trapped in the 5 : 3 resonance. After 120,000 yr, φ is circulating and the particle is no longer trapped in the 5 : 3 resonance. It does eventually become trapped in the 3 : 2 resonance, however. *Bottom:* Variation of the eccentricity with time for particle 1. The dashed line is the value of $e_{\max}$, the maximum value of eccentricity a particle trapped in the 5 : 3 resonance can reach. Note, however, that the particle's eccentricity becomes slightly higher than $e_{\max}$ while the particle is clearly still trapped in resonance. The theory to calculate $e_{\max}$ is only valid for low eccentricities since it is only to second order in e, so it is not surprising that the theory and the results do not agree completely.

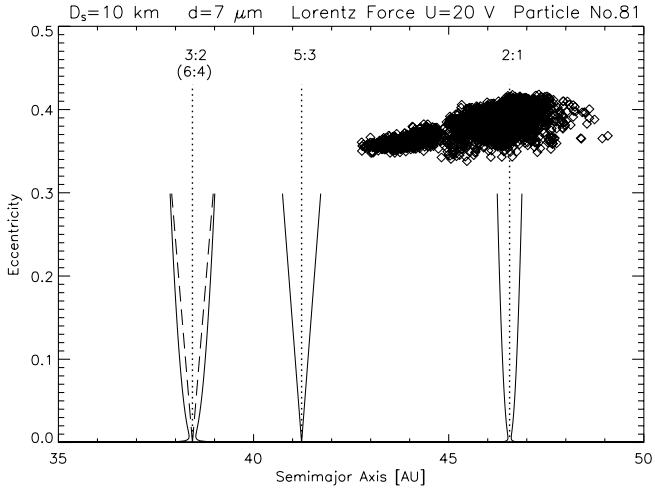

FIG. 17.—Eccentricity vs. semimajor axis for particle 81 in a RADAU run including the standard forces and the Lorentz force where $U = 20$ V. The run consists of 249 particles integrated for 250,000 yr and includes the effects of gravity, PR drag, solar wind corpuscular drag, radiation pressure, and the Lorentz force assuming that the particles have a potential, U, equal to 20 V. The 7 μm diameter particles ($\beta = 0.07104$) were released from a source body 10 km in diameter in a Pluto-like orbit. Each diamond represents the particle's orbital elements at 100 yr intervals. The 3 : 2, 5 : 3, and 2 : 1 libration widths are shown as solid lines, while the 6 : 4 libration width is shown as a dashed line. The exact location for each resonance is plotted as a dotted line. Particle 81 is trapped in the 2 : 1 resonance with Neptune.

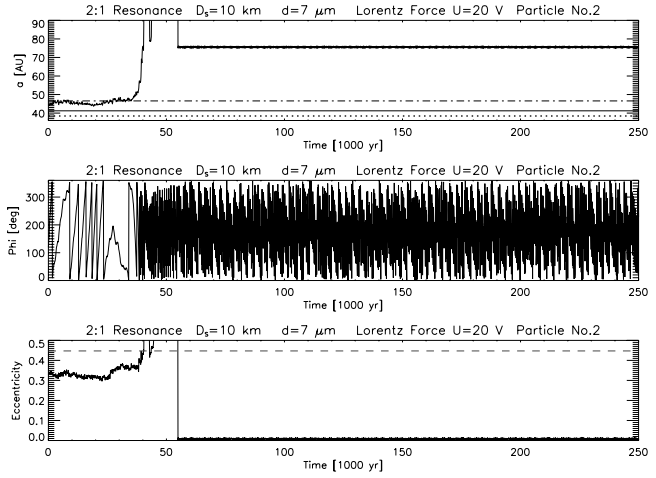

FIG. 18.—Variation of semimajor axis, resonant argument, and eccentricity with time for particle 2 in a RADAU run including the standard forces and the Lorentz force where $U = 20$ V. The run consists of 249 particles integrated for 250,000 yr and includes the effects of gravity, PR drag, solar wind corpuscular drag, radiation pressure, and the Lorentz force assuming that the particles have a potential, U, equal to 20 V. The 7 μm diameter particles ($\beta = 0.07104$) were released from a source body 10 km in diameter in a Pluto-like orbit. *Top:* Variation of semimajor axis, a, with time. The exact location for the 3 : 2 resonance for the $\beta = 0$ case is plotted as a dotted line. The exact locations of the 5 : 3 and 2 : 1 resonances are plotted as a solid line and a dot-dashed line, respectively. Particle 2 is initially trapped in the 2 : 1 resonance. Eventually, however, the particle achieves a parabolic or hyperbolic orbit and RADAU "excludes" it from the system by assigning it $a = 75$ AU and $e = 0$. *Middle:* Variation of the resonant argument for the 2 : 1 resonance (where $j_1 = 3$, $j_2 = -2$, $j_3 = -1$, $j_4 = 0$, $j_5 = 0$, and $j_6 = 0$) with time. The resonant argument is alternating between librating and circulating for the first 30,000–40,000 yr, before the particle becomes excluded from the system. *Bottom:* Particle's eccentricity appears to reach e_{max} shortly before the particle achieves a parabolic or hyperbolic orbit and is excluded from the system by RADAU.

example of which is shown in Figures 13 and 14. Upon ejection from the source body, radiation pressure exerts a strong influence on small particles and, as a result, many of them start out some distance away from 39.4 AU, allowing them to become initially trapped in other resonances. Another illustration of this point is in Figures 15 and 16, where it can be clearly seen that the particle starts out being trapped in the 5 : 3 resonance, reaches a maximum eccentricity, e_{max}, and then evolves out of the 5 : 3 resonance and eventually becomes trapped in the 3 : 2 resonance.

In Table 6 we see that significantly more particles are trapped in the 2 : 1 resonance in the $U = 20$ V Lorentz force case than in the standard forces case. Shown in Figure 17 is an example of a particle trapped in the 2 : 1 resonance for the $U = 20$ V Lorentz force case. The semimajor axis of the particle librates around the exact location of the 2 : 1 resonance. The resonant argument for the 2 : 1 resonance (where $j_1 = 2$, $j_2 = -1$, $j_3 = -1$, $j_4 = 0$, $j_5 = 0$, and $j_6 = 0$) is librating for approximately 200,000 yr, although for part of that time, φ seems to be circulating.

In addition, many of the particles in the $U = 20$ V Lorentz force case are eventually excluded from the numerical integrations as a result of the particles obtaining a high eccentricity and/or large semimajor axis (see Fig. 18). In fact, as shown in Table 6, in a comparison of runs with similar initial conditions (7 μm diameter particles originating from 10 km source bodies integrated for 250,000 yr with 249 particles in each run), $57\% \pm 8\%$ of the particles in the $U = 20$ V Lorentz force run were eventually excluded from the integrations, while none of the particles in any of the other runs were excluded.

In the case of the 6 : 4 and 5 : 3 resonances only one of the eccentricity resonances was considered. In the case of the 6 : 4 external resonance, we considered the case in which $j_1 = 6$, $j_2 = -4$, $j_3 = -2$, and $j_4 = j_5 = j_6 = 0$, and in the case of the 5 : 3 external resonance, we only considered the case in which $j_1 = 5$, $j_2 = -3$, $j_3 = -2$, and $j_4 = j_5 = j_6 = 0$. In the run without Lorentz forces, most of the particles became trapped in the 5 : 3 resonance. However, the addition of the Lorentz force with a high enough grain potential ($U = 20$ V) seems to scatter some particles out to larger semimajor axes, where they can become trapped in the 2 : 1 resonance, or smaller semimajor axes, where they can become trapped in the 3 : 2 resonance. In the case of the other runs including the Lorentz force with a U of 5 V and both with and without the effect of neutral interstellar gas drag included ($C_D = 1$) slightly less particles are trapped in the 5 : 3 and 2 : 1 resonances than in the standard forces run, which is to be expected for additional drag forces. These results are confirmed by a separate set of runs having 1017 particles each but the same initial conditions: 7 μm diameter particles originating from 10 km source bodies integrated for 250,000 yr (see Table 7).

For the 249 7 μm diameter particle standard forces run originating from 10 km diameter source bodies, we did check for trapping for all of the 5 : 3 external mean motion resonances. We did not find any particles trapped in the other eccentricity resonances, but we did find particles trapped in the inclination resonances (see Fig. 19). The percentages of particles trapped in all of the external 5 : 3 mean motion resonances for this particular run are listed in Table 8. The criteria for trapping are based on whether the resonant argument, φ, is librating. Recall equation (22), which gives $\varphi = j_1\lambda' + j_2\lambda_N + j_3\tilde{\omega}' + j_4\tilde{\omega}_N + j_5\Omega' + j_6\Omega_N$,

TABLE 7

A Comparison of Results for Numerical Runs (Consisting of 1017 Particles Each) for 7 μm Diameter Particles ($\beta = 0.07104$) Originating from 10 km Diameter Source Bodies

Numerical Run	Percentage of Particles Trapped in Resonance (%)			
	3:2	6:4	5:3	2:1
Standard forces	0.4 ± 50	0.0	28.3 ± 6	2.0 ± 22
Standard forces and Lorentz force ($U = 5$ V)	0.0	0.0	19.3 ± 7	0.1
Standard forces and Lorentz force ($U = 20$ V)	6.8 ± 12.0	0.4 ± 50	11.4 ± 9	16.0 ± 8

where the primed osculating elements are those of the dust particles and the unprimed elements subscripted with an "N" are Neptune's. As can be seen from Table 8, the assumption that the $\tilde{\omega}'$ eccentricity resonance was most important was correct as no particles are trapped in any of the other eccentricity resonances. This is expected as the eccentricities of the Plutino dust particles ($e' \approx 0.25$) are much greater than the eccentricity of Neptune ($e_N \approx 0.009$) and the strength of the resonance is a function of the eccentricity. Consequently, the particle is preferentially trapped in the strongest resonance or the resonance associated with the largest coefficient, in this case the ($j_1 = 5$, $j_2 = -3$, $j_3 = -2$, and $j_4 = j_5 = j_6 = 0$) resonance (Murray & Dermott 1999). A sizeable percentage of particles are trapped in the inclination resonances (some particles may be trapped in multiple resonances). An example of such a particle (trapped in the 5:3 resonance where $j_1 = 5$, $j_2 = -3$, $j_3 = 0$, $j_4 = 0$, $j_5 = -2$, and $j_6 = 0$) is shown in Figure 19. The inclination resonances are a topic for future study.

Finally, it is important to note that the Lorentz force could also create a structure similar in appearance to a dust band. The interplanetary solar magnetic field is composed of different sectors that alternate in polarity. The Lorentz force increases particle inclinations as a result of particles in low-inclination orbits experiencing a random walk in inclination due to both stochastic variations in solar magnetic field sector length and the alternating polarity of the sectors. As a result of this random walk, the inclination of a particle can increase over time as a result of the Lorentz force. Overall, this effect produces a dispersion in particle inclinations (Leinert & Grün 1990). The Lorentz force also causes a precession of nodes about the solar equator. Coupled with the dispersion in inclination, the structure will resemble a puffed-up ring of material (Gustafson 2000). However, this circumsolar ring is completely independent of the presence of planets in the system, unlike the resonant rings we have been discussing in this paper. Shown in Figure 20 are plots of the projection of the orbits of the particles onto the X- and Z-axes for the standard forces case and the $U = 5$ V Lorentz force case. Note how in the Lorentz force case the disk has a wider vertical extent.

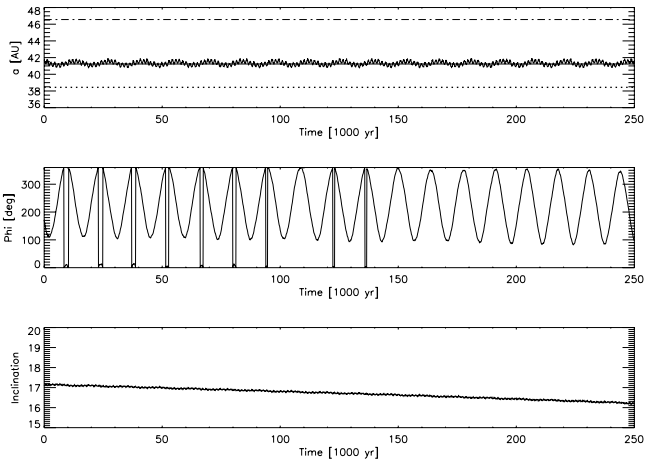

Fig. 19.—Variation of semimajor axis, resonant argument, and inclination with time for particle 8 in a 5:3 inclination resonance. The run includes the effects of gravity, PR drag, solar wind corpuscular drag, and radiation pressure. The 7 μm diameter particles ($\beta = 0.07104$) in this RADAU run were released from a 10 km source body. *Top:* Variation of semimajor axis, a, with time. The exact location for the 5:3 resonance is plotted as a solid line, the exact location of the 3:2 resonance is a dotted line, and the exact location of the 2:1 resonance is a dot-dashed line. *Middle:* Variation of the resonant argument for the 5:3 resonance (where $j_1 = 5$, $j_2 = -3$, $j_3 = 0$, $j_4 = 0$, $j_5 = -2$, and $j_6 = 0$) with time. The resonant argument is clearly librating. *Bottom:* Variation of the inclination of particle 8 with time.

8.3. *Neutral Interstellar Gas Drag*

Scherer (2000) does not take the Lorentz force into consideration and furthermore predicts that trapping of particles into mean motion resonances in the presence of neutral interstellar gas drag is very unlikely. In Figure 9, a full set of runs (for 4, 10, 20, 50, and 100 μm diameter particles, as well as the $\beta = 0$ case) with the Lorentz force ($U = 5$ V) and the neutral interstellar gas drag ($C_D = 1$) is shown. Also shown is a full set of runs including the Lorentz force ($U = 5$ V) and the neutral interstellar gas drag where $C_D = 2$. The results are not statistically different than the basic case, which does not include the Lorentz force or neutral gas drag, in contrast to the predictions of Scherer (2000). As far as the percentage of particles trapped in the 3:2 resonance is concerned, neutral gas drag does not appear to have an appreciable effect. However, if plots of

TABLE 8

Percentage of Particles in the 5:3 Resonances

j_1 λ'	j_2 λ_N	j_3 $\tilde{\omega}'$	j_4 $\tilde{\omega}_N$	j_5 Ω'	j_6 Ω_N	Percentage Trapped (%)
5	−3	−2	0	0	0	34.1 ± 11
5	−3	−1	−1	0	0	0.0
5	−3	0	−2	0	0	0.0
5	−3	0	0	−2	0	30.5 ± 11
5	−3	0	0	−1	−1	28.9 ± 12
5	−3	0	0	0	−2	25.7 ± 13

Notes.—Percentage of particles in the 5:3 resonances for a run consisting of 7 μm diameter particles ($\beta = 0.07104$) originating from 10 km diameter source bodies with the effects of gravity, PR drag, solar wind corpuscular drag, and radiation pressure included. The run contains 249 particles.

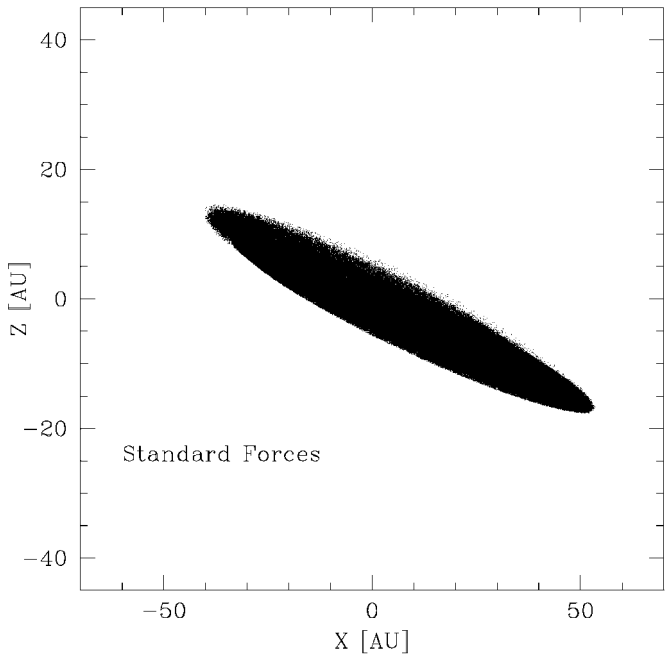

FIG. 20*a*

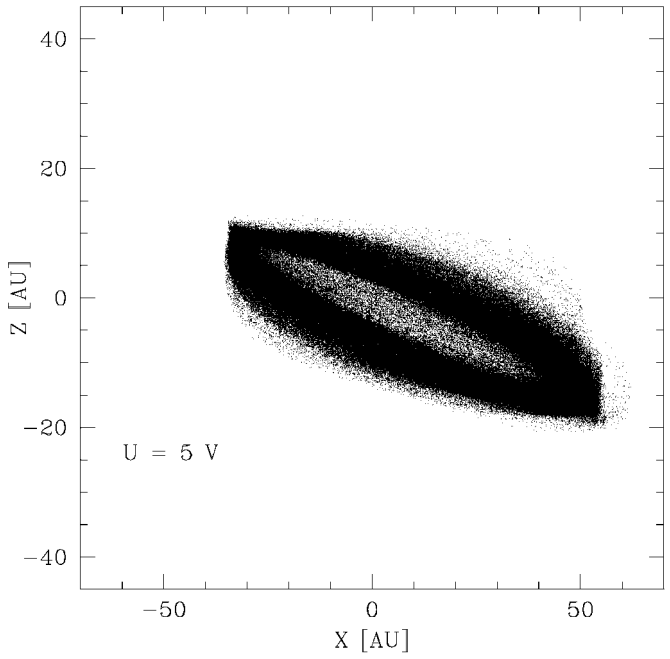

FIG. 20*b*

FIG. 20.—*X*-*Z* distribution of orbits for (*a*) the standard forces case and (*b*) the Lorentz force case where $U = 5$ V for the case of 7 μm diameter particles originating from 10 km diameter source bodies with 249 particles. The particles were integrated for 250,000 yr. Note how the particles have a broader vertical extent in the Lorentz force case, making the disk puffy. [*See the electronic edition of the Journal for a color version of Fig. 20b.*]

the projection of the orbits of the particles onto the *X*- and *Y*-axes are studied for the ISM plus Lorentz force case, the standard forces case, and both Lorentz force cases, the orbits look slightly different, with the neutral ISM case exhibiting a different shaped distribution in *X*-*Y* space. Plotted in Figure 21 are *X*-*Y* plots for the 7 μm diameter particle run ($\beta = 0.07104$), originating from 10 km diameter source bodies with 249 particles. The torus of dust for the $C_D = 1$ interstellar gas drag case seems "squashed" compared to the standard forces case and the $U = 5$ V Lorentz force case. In the case of the $U = 20$ V Lorentz force case, the orbits are scattered out to much larger ranges than the other runs. This reflects the fact that many of the particles eventually become excluded from the system.

9. SIZE-FREQUENCY DISTRIBUTION

Many theoretical questions remain about the size-frequency distribution of the dust particles in the entire Kuiper disk. The size-frequency distribution of the Kuiper Belt (or the asteroid belt) can be described by

$$\frac{dN}{dD} = D_0^p D^{-(p+1)} , \tag{47}$$

where D_0 is a constant, D is the diameter of the smallest particle being considered, dN is the number of particles in a bin of width dD, and p is a constant that indicates whether the particles are in collisional equilibrium, a state in which there is a balance between grain creation (by collisions) and grain removal (by radiation pressure, PR drag, mutual destructive collisions, and sublimation) from the system (Dermott et al. 1999). Equation (47) is for large bodies and is not expected to hold for the smallest particles (<1 μm) in the system, as a result of the effect of radiation pressure. The constant p can be written as

$$p \equiv 3(q - 1) , \tag{48}$$

where q is the size-frequency index. A system in collisional equilibrium has a size-frequency index of $q = 11/6 \approx 1.83$ and, correspondingly, a p equal to 2.5, assuming a single material strength (Dohnanyi 1969). The cumulative number of particles with diameters greater than D is given by

$$N_{\rm cum}(> D) = \frac{1}{p}\left(\frac{D_0}{D}\right)^p , \tag{49}$$

assuming that $D \ll D_{\rm max}$, where $D_{\rm max}$ is the diameter of the largest body in the distribution and $p > 1$, which is the case for collisional equilibrium. The distribution of area for the system can be written as

$$dA = \left(\frac{\pi}{4} D^2\right) dN , \tag{50}$$

where $\pi D^2/4$ is the area of an individual particle of diameter D. Integrating equation (50) from $D_{\rm min}$, the diameter of the smallest particles in the distribution, to $D_{\rm max}$ and using equation (47) yields

$$A_{\rm cum} = \int_{D_{\rm min}}^{D_{\rm max}} \frac{\pi}{4} D_0^p D^{-(p-1)} dD . \tag{51}$$

If $p > 2$, which is the case for collisional equilibrium, using equation (48), the cumulative surface area associated with this distribution can be written as

$$A_{\rm cum} = \frac{\pi D_{\rm min}^2}{4(3q - 5)} \left(\frac{D_0}{D_{\rm min}}\right)^{3(q-1)} . \tag{52}$$

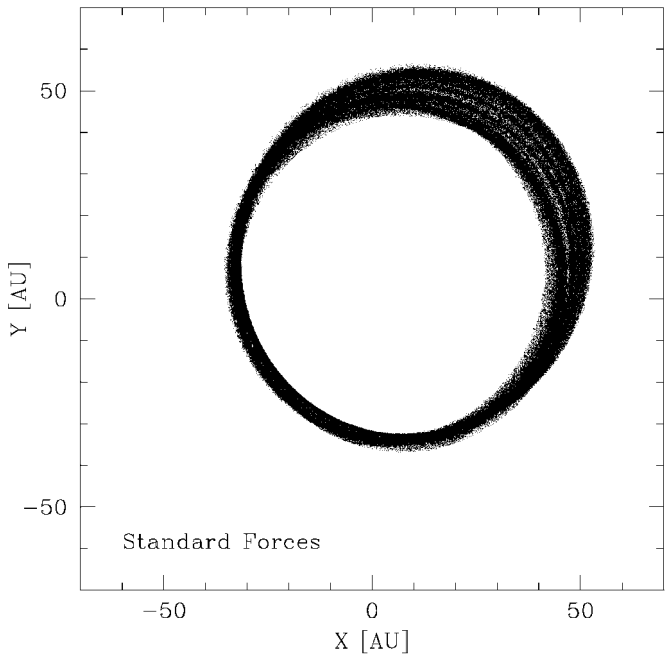

FIG. 21*a*

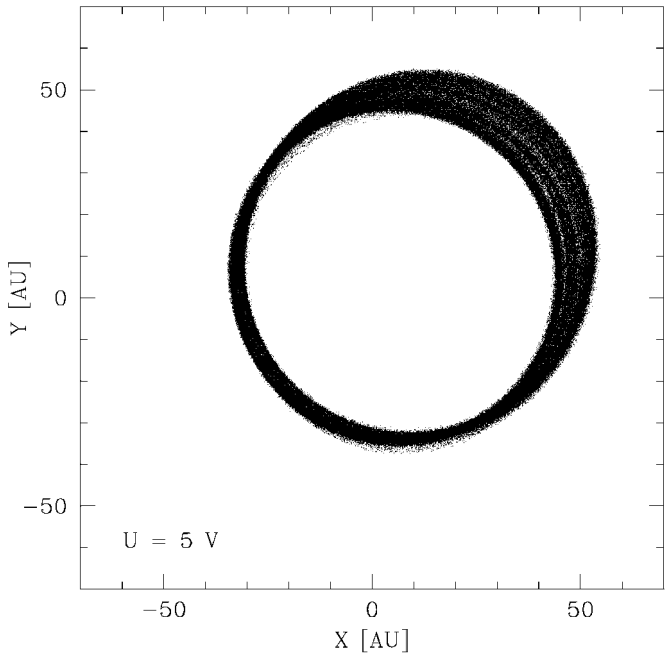

FIG. 21*b*

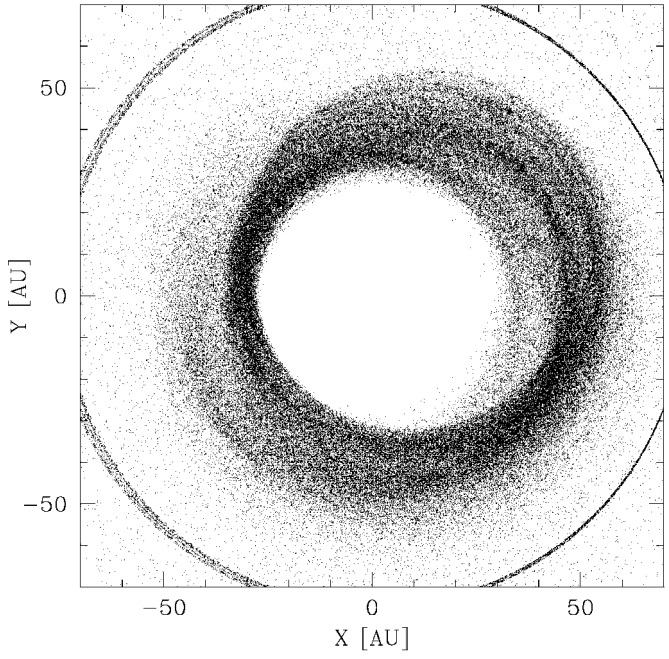

FIG. 21*c*

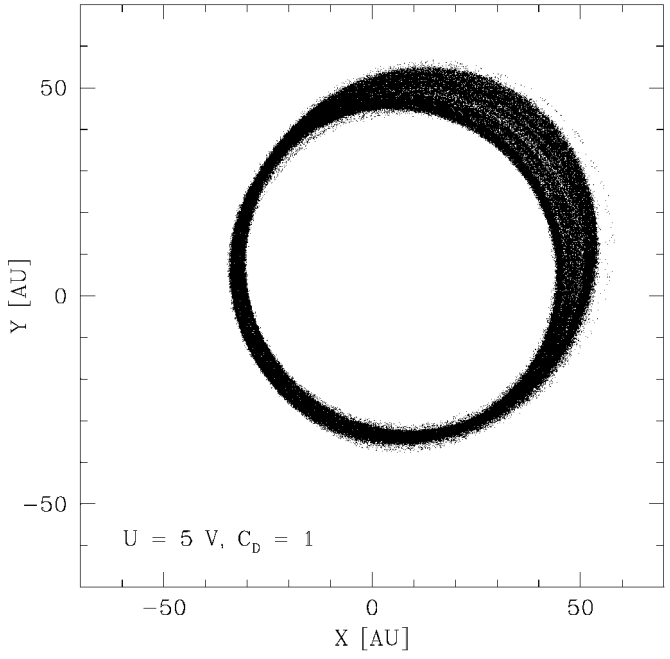

FIG. 21*d*

FIG. 21.—*X*-*Y* number density distribution of orbits for the standard forces case, both Lorentz force cases, and the neutral interstellar gas drag case for the case of 7 μm diameter particles originating from 10 km diameter source bodies with 249 particles. The particles were integrated for 250,000 yr, although only the first 100,000 yr are shown here. (*a*) Standard forces case. (*b*) Standard forces with the addition of the Lorentz force with a $U = 5$ V. (*c*) Standard forces with the addition of the Lorentz force ($U = 20$ V); the ring around 75 AU is due to an effect of the integrator "excluding" the particles. (*d*) Standard forces, the Lorentz force ($U = 5$ V), and the effects of neutral interstellar gas drag with $C_D = 1$. The dust torus appears slightly squashed in the interstellar gas drag case when all the orbits are plotted. [*See the electronic edition of the Journal for a color version of Figs. 21b–21d.*]

In this $p > 2$ case, the area is dominated by small particles and $A_{\rm cum}$ is independent of $D_{\rm max}$. If we assume that each particle has a mass, m_p, equal to $\pi\rho D^3/6$, where ρ is the density of a given particle, a cumulative mass, $M_{\rm cum}$, can be calculated from a mass increment $dM = m_p\, dN$. If $p < 3$, which is true for collisional equilibrium, then the mass is dominated by large particles and the cumulative mass can be expressed as

$$M_{\rm cum} = \frac{\pi\rho}{6} D_0^3 \frac{1}{(3-p)} \left(\frac{D_{\rm max}}{D_0}\right)^{(3-p)}. \qquad (53)$$

We can determine D_0 by assuming an appropriate value for $D_{\rm max}$, setting $M_{\rm cum}$ equal to the total mass of the system

for which the bodies have the same size-frequency index, and then solving equation (53) for D_0. For the case of collisional equilibrium, $D_{\max}$ is the size of the largest body still in collisional equilibrium and $M_{\rm cum}$ is the total mass of the system for bodies with diameters in the range from $D_{\min}$ to $D_{\max}$.

9.1. *Zodiacal Cloud*

This method for calculating cumulative area is appropriate for the solar system dust bands and the background zodiacal cloud since all of the crucial parameters (q, $D_{\max}$, and $M_{\rm cum}$) are well constrained. The dust bands were discovered by the *Infrared Astronomical Satellite* (*IRAS*; Low et al. 1984) and have been attributed to the breakup of three Hirayama asteroid families: Eos, Themis, and Koronis (Dermott et al. 1984), although Veritas may also play a role in contributing to the dust band emission (Nesvorný et al. 2002; Dermott et al. 2002). For the dust band associated with Eos, for example, $D_{\max}$ and $M_{\rm cum}$ are the diameter and mass of the Eos asteroid, and q was determined to be less than or equal to approximately 1.4 (and $p \approx 1.2$) by Grogan, Dermott, & Durda (2001). Since $p < 3$ ($q < 2$), the mass is dominated by the large particles. Leinert & Grün (1990) estimate the mass of the zodiacal cloud to be 10^{16}–10^{17} kg, and we take $M_{\rm cum}$ to be 10^{16} kg, noting that the area and brightness of the cloud scale linearly with $M_{\rm cum}$. For our maximum particle size, $D_{\max}$, we assume 500 μm (Wyatt et al. 1999). Since q for the asteroid belt is 1.4, the distribution is weighted toward the larger particles and we are justified in simply creating a model cloud composed entirely of 500 μm diameter particles to get a lower limit to the expected brightness of the zodiacal cloud. From these assumptions, we calculate $A_{\rm cum}$ for the zodiacal cloud. We take $D_{\max}$ to be 500 μm. We take the number of particles in the disk to be $N_{\rm cum} = M_{\rm cum}/m_p$, where m_p is the mass of an individual 500 μm diameter spherical dust particle with density $\rho = 2500$ kg m^{-3}. Given that $A_{\rm cum} = \pi D^2 N_{\rm cum}/4$, where $D = D_{\max}$, we derive a cumulative area $A_{\rm cum} = 1.2 \times 10^{10}$ km^2.

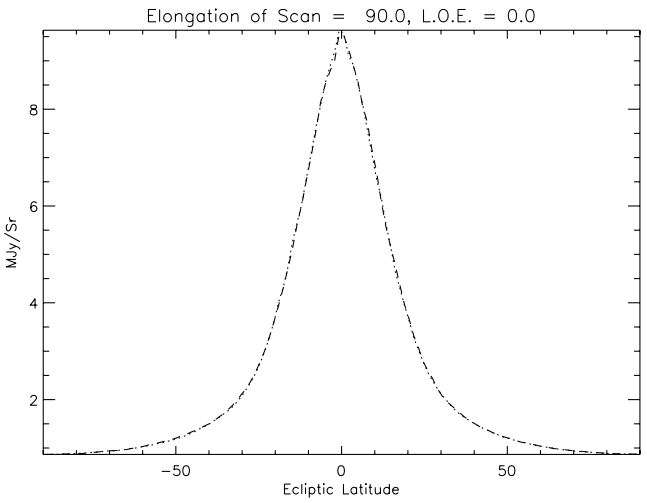

FIG. 22.—Scan in ecliptic latitude of the brightness of the zodiacal cloud model at a solar elongation angle $\epsilon = 90°$ in the 60 μm wave band. The model is of a simple asteroidal background cloud with no brightness asymmetries ranging from 1 to 3 AU having a total area equal to $A_{\rm cum} = 1.2 \times 10^{10}$ km^2. The peak of the brightness at an ecliptic longitude of approximately 0° is approximately 9.5 MJy sr^{-1}.

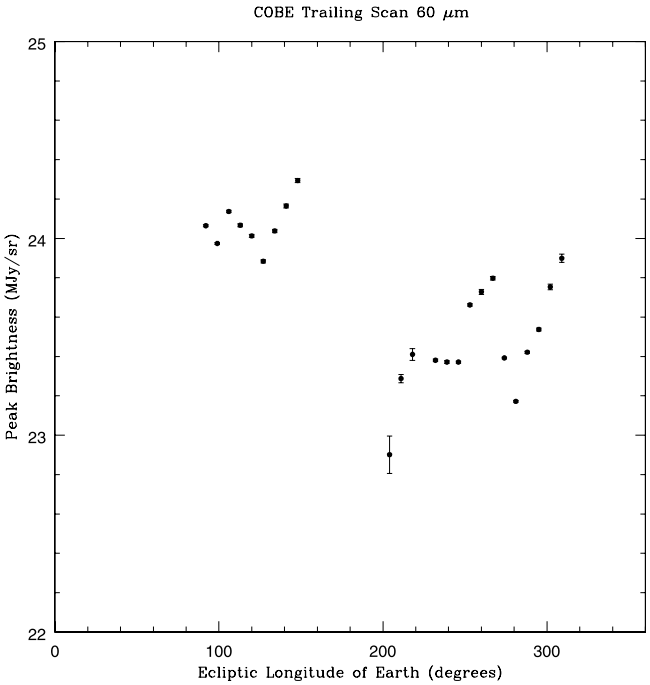

FIG. 23.—*COBE* data trailing scan at 60 μm. This figure shows a plot of the peak brightness at a solar elongation angle of 90° vs. ecliptic LoE for the 60 μm *COBE* DIRBE wave band for data taken in the direction trailing the Earth in its orbit.

We then build a model of a simple background zodiacal cloud with no brightness asymmetries. The radial extent of the cloud is from 1 to 3 AU, and the particles populate the disk according to a $1/r$ PR drag distribution. The total area in the model is set to $A_{\rm cum} = 1.2 \times 10^{10}$ km^2. Based on these input parameters, orbits of the particles are generated and then distributed through a three-dimensional array of cells forming a SIMUL model (for additional information on

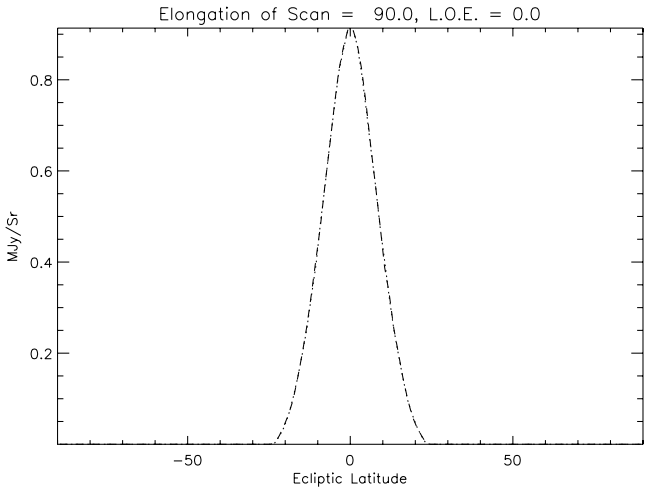

FIG. 24.—Scan in ecliptic latitude of the brightness of the Kuiper disk model cloud at a solar elongation angle $\epsilon = 90°$ in the 60 μm wave band. The model is of a simple Kuiper disk with no brightness asymmetries ranging from 30 to 50 AU having a total area equal to $A_{\rm cum} = 8.87 \times 10^{13}$ km^2. The peak of the brightness at an ecliptic longitude of approximately 0° is approximately 0.97 MJy sr^{-1}, which is much closer to the range of limits found in Teplitz et al. (1999) and also agrees with Fig. 1 of Backman et al. (1995) to within a factor of ~3.

SIMUL, a zodiacal cloud simulation tool developed at the University of Florida, see Dermott et al. 1988b; Grogan et al. 2001). Assuming that the particles are composed of astronomical silicate, a line-of-sight integrator creates a scan in ecliptic latitude of the brightness of the zodiacal cloud model at a solar elongation angle $\epsilon = 90^\circ$ in the 60 μm wave band (see Fig. 22). Note that, in contrast to other models (e.g., the Kelsall et al. 1998 model), we are not fitting an empirically derived model to the data. We are instead constructing models based on physical assumptions about the grain distribution in the zodiacal cloud. The peak of the brightness at an LoE of 0° is approximately 9.5 MJy sr^{-1}. If we use $M_{\rm cum} = 10^{17}$ kg, then the peak brightness of the model is approximately 95 MJy sr^{-1}. The *COBE* DIRBE observed peak brightness in the 60 μm wave band in the direction trailing the Earth is approximately 23.5 MJy sr^{-1}, which fits in well with our predicted brightnesses (see Fig. 23). (Given that s is the particle radius, the emissivity is unity for $\lambda \leq 2\pi s$, making the grain a good emitter for the wavelength λ. For $\lambda \geq 2\pi s$, the grain emissivity is less than 1.)

9.2. *Kuiper Disk*

In contrast to the case of the zodiacal cloud, the size-frequency distribution of KBOs and the dust in the Kuiper disk is poorly constrained. Only ~650 KBOs have been discovered to date (Parker 2003), compared to several thousand asteroids, so the values for $D_{\rm max}$ and $M_{\rm cum}$ are significantly more uncertain for the Kuiper Belt than they are for the asteroid belt. This allows for a very wide range of D_0, on which $A_{\rm cum}$ and the surface brightness of the cloud are highly dependent. It is not known if the Kuiper Belt is in collisional equilibrium, which means that the constraints on q

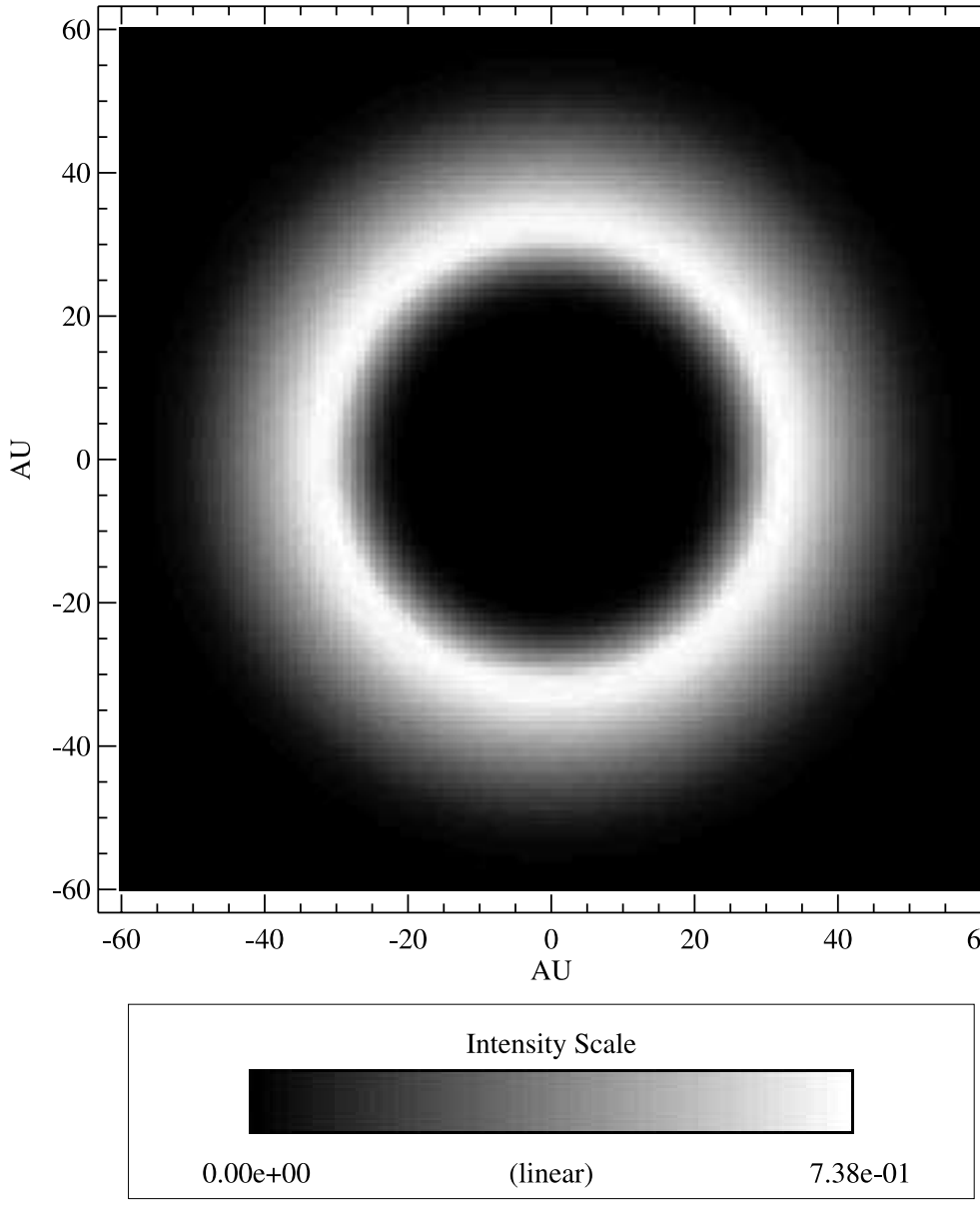

FIG. 25.—SIMUL model of a simple Kuiper disk with no brightness asymmetries ranging from 30 to 50 AU having a total area equal to $A_{\rm cum} = 8.87 \times 10^{13}$ km^2. This is a face-on view of the model as it would appear to an exosolar observer at 7.8 pc in the 60 μm wave band. [*See the electronic edition of the Journal for a color version of this figure*.]

are also poor. Jewitt, Luu, & Trujillo (1998) estimated the size-frequency index of the KBOs to be $1.83 \leq q \leq 2.17$. The lower limit is the value of q for collisional equilibrium. However, the size-frequency index of the KBOs may not be the same as the size-frequency index of the small grains in the disk.

Despite these obvious difficulties, we attempt to calculate the surface brightness of the Kuiper disk by making some reasonable choices for $M_{\rm cum}$, $D_{\rm max}$, and q. We set $M_{\rm cum}$ to the total mass of dust in the Kuiper Belt, which is estimated to be $1 \times 10^{-5} M_{\oplus}$ (Backman et al. 1995). Since the q of the Kuiper disk is unconstrained, we assume that, like the zodiacal cloud, the size-frequency distribution of the Kuiper disk is heavily weighted toward the large particles and we assume that our entire Kuiper disk is composed of 500 μm diameter particles composed of astronomical silicate. We take $D_{\rm max} = 500$ μm and the number of particles in the disk to be $N_{\rm cum} = M_{\rm cum}/m_p$, where m_p is the mass of an individual 500 μm diameter spherical dust particle with density $\rho = 2030$ kg m^{-3}. Given that $A_{\rm cum} = \pi D^2 N_{\rm cum}/4$, where $D = D_{\rm max}$, we calculate a cumulative area for the Kuiper disk of $A_{\rm cum} = 8.87 \times 10^{13}$ km^2. We then build a SIMUL model of a simple Kuiper disk with no brightness asymmetries ranging from 30 to 50 AU in radial extent and having a total area equal to $A_{\rm cum} = 8.87 \times 10^{13}$ km^2. The particles populate the disk according to a $1/r$ PR drag distribution. Based on these input parameters, orbits of the particles are calculated and then distributed through a three-dimensional array of cells forming a SIMUL model. We perform a scan in ecliptic latitude of the brightness of the cloud at an elongation angle $\epsilon = 90°$ in the 60 μm wave band (see Fig. 24). The peak of the brightness at LoE $= 0°$ is approximately 0.97 MJy sr^{-1}. A face-on view of the SIMUL model as it would appear to an exosolar observer is shown in Figure 25.

The Kuiper dust disk is predicted to be, at most, a few percent of the brightness of the zodiacal cloud (Backman et al. 1995; Teplitz et al. 1999) from *COBE* upper limits. For the 60 μm wave band, Teplitz et al. (1999) report four different upper limits for the total signal from the Kuiper Belt, $I_{\rm KB}(\nu)$. The upper limits on the total brightness range from 0.3 to 16.0 MJy sr^{-1} (Teplitz et al. 1999). The 16 MJy sr^{-1} limit is merely the full *COBE* DIRBE infrared signal in the 60 μm wave band given in Figure 2 of Backman et al. (1995) at an ecliptic latitude of $-19\overset{\circ}{.}1$. The particular latitude is chosen because Teplitz et al. (1999) assume that the Kuiper disk density distribution is constant to $\pm 19\overset{\circ}{.}1$ in ecliptic latitude and zero outside that range. The data were taken from the DIRBE annual average data set (Backman et al. 1995). The contribution from the foreground zodiacal cloud was not removed from the *COBE* DIRBE infrared signal, making this limit a poor constraint on $I_{\rm KB}(\nu)$; that is, the signal from the Kuiper disk should be much lower than 16 MJy sr^{-1}. The other limits of 0.3, 1.50, and 0.75 MJy sr^{-1} were obtained in the following fashion. The 1.50 MJy sr^{-1} limit is a 2 σ limit found by Hauser et al. (1998), while the 0.75 MJy sr^{-1} value was a standard deviation given by Hauser et al. (1998). The smallest limit, $I_{\rm KB}(\nu) = 0.3$ MJy sr^{-1}, was obtained by the subtraction of the component of the *COBE* data due to asteroidal emission using the Reach (1988) zodiacal cloud model (Backman et al. 1995).

The peak brightness in Figure 24 of approximately 0.97 MJy sr^{-1} is well within the range of limits found in Teplitz et al. (1999) and also agrees with Figure 1 of Backman et al. (1995) to within a factor of $\sim$3. A Kuiper disk composed of 500 μm diameter particles fits well with upper limits and other Kuiper disk models. In addition, this has implications for how easy it will be to observe the Kuiper disk brightness asymmetry. A disk with a size-frequency distribution weighted toward small particles, which are not trapped in resonance, will have a washed-out resonant signature, but a disk heavily weighted toward large particles, which are more likely to become trapped, may have a stronger, more easily identifiable double-lobed structure. However, it should be noted that models of the Kuiper disk made with $q = 1.83$ grossly overpredicted the Kuiper disk brightness (Holmes 2002). Changing q by a small amount, on the order of ± 0.4, can change the predicted brightness of the cloud by several orders of magnitude (see Fig. 26). Much observational work still needs to be done to better determine $M_{\rm cum}$, $D_{\rm max}$, q, and the albedo for the KBOs, which will aid future modeling efforts.

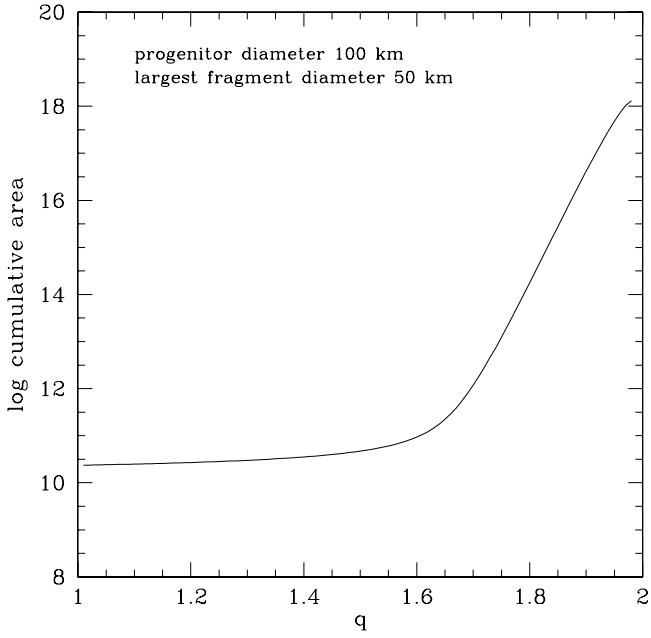

FIG. 26.—Illustration of the dramatic effect of the size-frequency distribution index q on the cumulative area of material resulting from the disruption of a parent body, here assumed to be 100 km in diameter. Below $q = 5/3$, the total area is dominated by the contribution from the large particles in the distribution; above $q = 5/3$, the area is dominated by the small particles. In this small-particle regime, modest changes in q can result in order-of-magnitude differences in the cumulative area and hence the brightness of the distribution.

10. CONCLUSIONS

The probability that the Kuiper disk particles remain in (or are later recaptured into) the 3:2 mean motion resonance increases with decreasing β (i.e., increasing particle size). For the standard forces cases, none of the 4 μm ($\beta = 0.12928$) particles were in the 3:2 resonance. In the other cases, only 0%–0.8% of the 4 μm particles were in the 3:2 resonance. In contrast, for the $\beta = 0$ case, 98.8%–100% (0 and 10 km source bodies) and 68.7%–75.9% (100 km source body) of the particles were in resonance for at least part of the 250,000 yr integration. Consequently, a size distribution for the Plutino

disk must be weighted toward larger particles, with a cutoff for small particles in the resonance at approximately 4 μm. It is of course possible to have a population of small particles that are drifting through the libration width and are not in resonance or that are generated via a collisional cascade by larger particles. However, some of the small particles initially removed from the libration width by radiation pressure can eventually evolve back into the libration width through PR drag and become trapped in resonance.

When combined with the size-frequency distribution of the entire disk, the lack of small particles in resonance may help to explain why the Kuiper disk is so faint. If a Plutino disk is lacking in small particles, it will be deficient in surface area and consequently less bright than a nondepleted disk. Our results from § 9 support this idea: the total brightness of the Kuiper disk is fitted reasonably well by a Kuiper disk composed solely of large particles, implying a q lower than 1.83. A disk weighted toward large particles will have a stronger, more easily identifiable resonant signature than a disk in collisional equilibrium.

Finally, as long as the potential, U, of the particles is small ($U \approx 5$ V), the Lorentz force does not seem to inhibit trapping into mean motion resonances. However, it should be noted that if the grains in an exosolar system have a high potential, then the Lorentz force would have a strong effect in that system. It is also important to keep in mind that the Lorentz force could create a structure resembling a puffed-up ring of material (Gustafson 2000) that would be independent of the presence of planets in the system. It would be important, therefore, to distinguish this uniform puffed torus from resonant rings that are linked to the presence of planets in a system.

This research was funded in part by a NASA GSRP grant. SIMUL was developed at the University of Florida by the Solar System Dynamics Group led by S. F. Dermott. Part of the research described in this publication was carried out at the Jet Propulsion Laboratory, California Institute of Technology, under a contract with the National Aeronautics and Space Administration. HiRes image processing was performed by Tim Thompson at JPL.

REFERENCES

Backman, D. E., Dasgupta, A., & Stencel, R. E. 1995, ApJ, 450, L35
Backman, D. E., & Paresce, F. 1993, in Protostars and Planets III, ed. E. H. Levy & J. I. Lunine (Tucson: Univ. Arizona Press), 1253
Bertin, P., Lallement, R., Ferlet, R., & Vidal-Madjar, A. 1993, J. Geophys. Res., 98, 15193
Brouwer, D., & Clemence, G. M. 1961, Methods of Celestial Mechanics (New York: Academic Press)
Burns, J. A., Lamy, P. L., & Soter, S. 1979, Icarus, 40, 1
Cellino, A., Michel, P., Tanga, P., Zappalà, V., Paolicchi, P., & Dell'Oro, A. 1999, Icarus, 141, 79
Dermott, S. F., Grogan, K., Holmes, E., & Kortenkamp, S. 1999, in Formulation and Evolution of Solids in Space, ed. J. M. Greenberg & A. Li (Dordrecht: Kluwer), 565
Dermott, S. F., Grogan, K., Holmes, E. K., & Wyatt, M. C. 1998, in Exozodiacal Dust Workshop Conference Proceedings, ed. D. E. Backman, L. J. Caroff, S. A. Sandford, & D. H. Wooden (Moffett Field: NASA), 59
Dermott, S. F., Jayaraman, S., Xu, Y. L., Gustafson, B. Å. S., & Liou, J. C. 1994b, Nature, 369, 719
Dermott, S. F., Kehoe, T. J., Durda, D., Grogan, K., & Nesvorný, D. 2002, in Proceedings of the Conference Asteroids, Comets, Meteors ACM 2002 (ESA SP-500; Noordwijk: ESA), 319
Dermott, S. F., Malhotra, R., & Murray, C. D. 1988a, Icarus, 76, 295
Dermott, S. F., Nicholson, P. D., Burns, J. A., & Houck, J. R. 1984, Nature, 312, 505
Dermott, S. F., Nicholson, P. D., Kim, Y., & Wolven, B. 1988b, in Comets to Cosmology, Proceedings of the Third *IRAS* Conference, ed. A. Lawrence (Berlin: Springer), 3
Dohnanyi, J. S. 1969, J. Geophys. Res., 74, 2531
Draine, B. T., & Lee, H. M. 1984, ApJ, 285, 89
Edgeworth, K. E. 1943, J. British Astron. Assoc., 53, 181
Everhart, E. 1989, in Dynamics of Comets: Their Origin and Evolution, ed. A. Carusi & G. B. Valeschhi (Dordrecht: Reidel), 185
Gehrels, N., & Chen, W. 1993, Nature, 361, 706
Geiss, J., Gloeckler, G., & Mall, U. 1994, A&A, 289, 933
Giblin, I. 1998, Planet. Space Sci., 46, 921
Gloeckler, G., et al. 1993, Science, 261, 70
Goertz, C. K. 1989, Rev. Geophys., 27, 271
Grogan, K., Dermott, S. F., & Durda, D. 2001, Icarus, 152, 251
Grogan, K., Dermott, S. F., & Gustafson, B. Å. S. 1996, ApJ, 472, 812
Grün, E., Gustafson, B. Å. S., Mann, I., Baguhl, M., Morfill, G. E., Staubach, P., Taylor, A., & Zook, H. A. 1994, A&A, 286, 915
Gustafson, B. Å. S. 1994, Annu. Rev. Earth Planet. Sci., 22, 553
———. 2000, IAU JD 4E, 11G
Gustafson, B. Å. S., Greenberg, J. M., Kolokolova, L., Xu, Y. L., & Stognienko, R. 2001, in Interplanetary Dust, ed. E. Grün, B. Å. S. Gustafson, S. F. Dermott, & H. Fechtig (Heidelberg: Springer), 509
Gustafson, B. Å. S., Grün, E., Dermott, S. F., & Durda, D. D. 1992, in Asteroids, Comets, Meteors 1991, ed. A. W. Harris & E. Bowell (Houston: Lunar and Planetary Institute), 223
Gustafson, B. Å. S., & Misconi, N. Y. 1979, Nature, 282, 276
Hauser, M. G., et al. 1998, ApJ, 508, 25
Holmes, E. K. 2002, Ph.D. thesis, Univ. Florida
Holsapple, K., Giblin, I., Housen, K., Nakamura, A., & Ryan, E. 2003, in Asteroids III, ed. W. F. Bottke, A. Cellino, P. Paolicchi, & R. P. Binzel (Tucson: Univ. Arizona Press), 443
Jackson, A. A., & Zook, H. A. 1992, Icarus, 97, 70
Jayaraman, S. 1995, Ph.D. thesis, Univ. Florida
Jewitt, D. C. 1999, Annu. Rev. Earth Planet. Sci., 27, 287
Jewitt, D. C., & Luu, J. X. 1993, Nature, 362, 730
Jewitt, D. C., Luu, J. X., & Trujillo, C. 1998, AJ, 115, 2125
Kelsall, T., et al. 1998, ApJ, 508, 44
Klacka, J. 1992, Earth Moon Planets, 59, 41
Kuiper, G. P. 1951, in Astrophysics, ed. J. A. Hynek (New York: McGraw-Hill), 357
Landgraf, M., Liou, J.-C., Zook, H. A., & Grün, E. 2002, AJ, 123, 2857
Leinert, C., & Grün, E. 1990, in IAU Colloq. 150, Physics and Chemistry in Space: Physics of the Inner Heliosphere I, ed. R. Schween & E. Marsch (Berlin: Springer), 207
Liou, J.-C., & Zook, H. A. 1999, AJ, 118, 580
Liou, J.-C., Zook, H. A., & Dermott, S. F. 1996, Icarus, 124, 429
Low, F. J., et al. 1984, ApJ, 278, L19
Luu, J., Marsden, B. G., Jewitt, D. Trujillo, C. A., Hergenrother, C. W., Chen, J., & Offutt, W. B. 1997, Nature, 387, 573
Malhotra, R., & Williams, J. G. 1998, in Pluto and Charon, ed. S. A. Stern & D. Tholen (Tucson: Univ. Arizona Press), 127
Miller, J. K., et al. 2002, Icarus, 155, 3
Moro-Martín, A., & Malhotra, R. 2002, AJ, 124, 2305
Murray, C. D., & Dermott, S. F. 1999, Solar System Dynamics (Cambridge: Cambridge Univ. Press)
Nesvorný, D., Bottke, W. F., Dones, L., & Levison, H. E. 2002, Nature, 417, 720
Parker, E. N. 1958, ApJ, 128, 664
Parker, J. W. 2003, Distant EKOs: The Kuiper Belt Electron. Newsl. 28
Pepin, R. O., Palma, R. L., & Schlutter, D. J. 2001, Meteoritics Planet. Sci., 36, 1515
Poynting, J. H. 1903, Philos. Trans. R. Soc. London, A202, 525
Reach, W. T. 1988, ApJ, 335, 468
Robertson, H. P. 1937, MNRAS, 97, 423
Scheeres, D. J., Durda, D. D., & Geissler, P. E. 2003, in Asteroids III, ed. W. F. Bottke, A. Cellino, P. Paolicchi, & R. P. Binzel (Tucson: Univ. Arizona Press), 527
Scherer, K. 2000, J. Geophys. Res., 105, 10329
Stern, S. A. 1996, A&A, 310, 999
Teplitz, V. L., Stern, S. A., Anderson, J. D., Rosenbaum, D., Scalise, R. J., & Wentzler, P. 1999, ApJ, 516, 425
Trujillo, C. A., & Brown, M. E. 2002, ApJ, 566, L125
Trujillo, C. A., Jewitt, D. C., & Luu, J. X. 2000, ApJ, 529, L103
US Naval Observatory and Royal Greenwich Observatory. 2001, The Astronomical Almanac for the Year 2001 (Washington: GPO)
Veverka, J., et al. 2001, Nature, 413, 390
Weidenschilling, S. J., & Jackson, A. A. 1993, Icarus, 104, 244
Witte, M., Rosenbauer, H., Banaszkiewicz, M., & Fahr, H. 1993, Adv. Space Res., 13(6), 121
Wyatt, M. C., Dermott, S. F., Telesco, C. M., Fisher, R. S., Grogan, K., Holmes, E. K., & Piña, R. K. 1999, ApJ, 527, 918
Wyatt, S. P., & Whipple, F. L. 1950, ApJ, 111, 134
Yamamoto, S., & Mukai, T. 1998, A&A, 329, 785
Yeomans, D. K., et al. 2000, Science, 289, 2085
Zappala, V., Farinella, P., Knezevic, & Paolicchi, P. 1984, Icarus, 59, 261